SAND2010-6613C

Aerodynamic and Acoustic Corrections for a Kevlar-Walled Anechoic Wind Tunnel

William J. Devenport[1], Ricardo A. Burdisso[2] and Aurelien Borgoltz[3]
Virginia Tech, Blacksburg, VA 24061, U.S.A.

Patricio Ravetta[4]
AVEC Inc., Blacksburg, VA 24060, U.S.A.

and

Matthew F. Barone[5]
Sandia National Laboratories[6], Albuquerque, NM 87185, U.S.A

The aerodynamic and acoustic performance of a Kevlar-walled anechoic wind tunnel test section has been analyzed. Aerodynamic measurements and panel method calculations were performed on a series of airfoils to reveal the influence of the test section walls, including their porosity and flexibility. A lift interference correction method was developed from first principles which shows consistently high accuracy when measurements are compared to viscous free-flight calculations. Interference corrections are an order of magnitude smaller than those associated with an open jet test section. Blockage corrections are found to be a fraction of those which would be associated with a hard-wall test section of the same size, and are negligible in most cases. New measurements showing the acoustic transparency of the Kevlar and the quality of the anechoic environment in the chambers are presented, along with benchmark trailing edge noise measurements.

I. Introduction

THIS paper presents the results of experimental, theoretical and computational studies of the aerodynamics and acoustics of a wind tunnel test section with acoustically transparent walls made from tensioned Kevlar cloth. In this novel test section design, originally implemented in the Virginia Tech 1.8m×1.8m Stability Tunnel and now also in the Japan Aerospace Exploration Agency 2m×2m wind tunnel, the Kevlar cloth contains the test section flow and separates it from the surrounding anechoic chamber(s). This arrangement promises a substantial reduction in aerodynamic interference when compared to the more conventional open-jet configuration used in most aeroacoustic wind tunnels. It also eliminates the need for a jet catcher and provides a practical model for extending the capabilities of conventional aerodynamic tunnels to include far-field acoustic measurements.

Remillieux *et al.* (2008) and Smith *et al.* (2005) describe the development of the Kevlar-walled acoustic test section and anechoic chamber system for the Virginia Tech Stability Wind Tunnel. They describe the initial performance of the facility including detailed results such as improvements in the acoustic environment, the behavior of the test section boundary layer, the deflections and pressures acting on the Kevlar windows. They also give initial results on the acoustic transparency of the Kevlar windows and their apparent effects on the lift interference on an airfoil model, inferred by comparison with inviscid free-flight calculations, as well as initial acoustic maps of trailing edge noise. Ito *et al.* (2010) describe the development of the acoustic system for the JAXA

[1] Professor, Department of Aerospace and Ocean Engineering, 215 Randolph Hall, Associate Fellow.
[2] Professor, Department of Mechanical Engineering, 100S Randolph Hall, Associate Fellow.
[3] Research Scientist, Department of Aerospace and Ocean Engineering, 215 Randolph Hall, Member.
[4] Chief Research Engineer, Senior Member.
[5] Senior Member of the Technical Staff, Wind and Water Power Technologies Department, MS 1124, Senior Member.
[6] Sandia is a multiprogram laboratory operated by Sandia Corporation, a Lockheed Martin Company, for the United States Department of Energy's National Nuclear Security Administration under Contract DE-AC04-94AL85000.

2m by 2m tunnel along with comparative measurements made using a high lift wing in the Stability Tunnel, the JAXA facility and an equivalent hard-wall configuration.

The results of Remillieux *et al.* (2009) were generally encouraging, showing lift interference effects significantly less than for a free jet and trailing edge noise levels broadly consistent with previous results. They did not, however, provide very detailed acoustic or aerodynamic comparisons or a clear understanding of the aerodynamic boundary conditions imposed by the Kevlar walls. In particular, if Kevlar-walled test sections of this type are to be routinely used for aeroacoustic testing, then an *a priori* method for the prediction of aerodynamic interference effects is needed.

In this paper we provide many of the missing details. We show detailed comparisons of measurements of trailing edge noise with the benchmark results of Brooks *et al.* (1989). We provide new measurements showing the acoustic transparency of the Kevlar and the quality of the anechoic environment in the chambers. We present aerodynamic measurements for a range of airfoils, and describe panel method calculations of aerodynamic performance in the test section, including the effects of Kevlar porosity and deflection. We develop from first principles an *a priori* method for predicting lift interference which shows consistently high accuracy when measurements are compared to viscous free-flight calculations. Interestingly, the interference corrections are only about half as large as those inferred by Remillieux *et al.* and an order of magnitude smaller than those associated with an open jet test section. Blockage corrections are also examined and found to be negligible except for the largest model. In this case the blockage correction is a fraction of that which would be associated with a hard-wall test section of the same size.

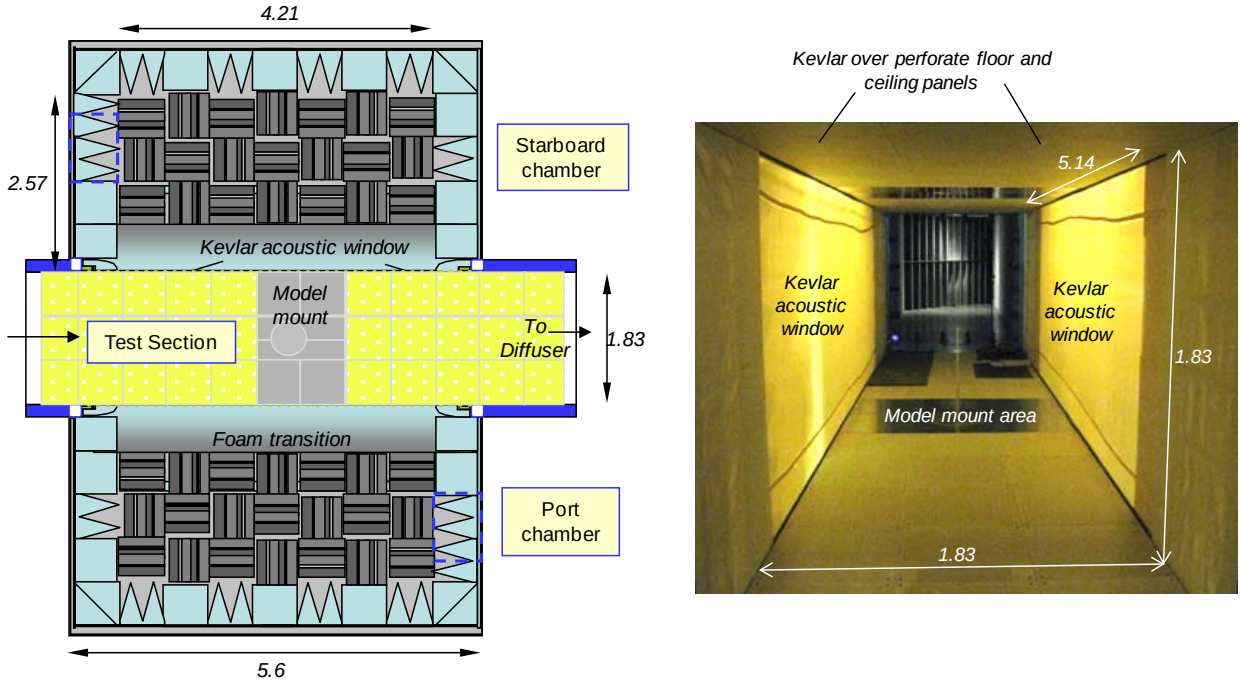

Figure 1. *VT Stability Wind Tunnel Anechoic System. Dimensions in meters. Left: cross section through the anechoic test section and chambers as seen from above. Right: Photograph taken from upstream showing the*

II. The Acoustic Test Section and Anechoic Chambers

A. Overall Description

The 1.83x1.83-m acoustic test section and anechoic chambers of the Virginia Tech Stability Wind Tunnel are depicted in Figure 1 (see Remillieux *et al.* for a description of the rest of the facility). The test section consists of acoustically treated upper and lower walls that run the full 7.3-m length of the test section and partial side walls, also treated, at the test section entrance and exit. Large rectangular openings in the side walls which extend 5.14m in the streamwise direction and cover the full 1.83-m height of the test section serve as acoustic windows. Sound generated in the test flow exits the test section through these into the anechoic chambers on either side. Large tensioned panels of Kevlar cloth cover these openings permitting the sound to pass while containing the bulk of the flow. The test section arrangement thus simulates a half-open jet, acoustically speaking. The Kevlar windows eliminate the need

for a jet catcher and, by containing the flow, substantially reduce the lift interference when airfoil models are placed in the test flow.

The upper wall of the test section is formed from a series of perforated metal panels bonded to a layer of Kevlar cloth that forms a smooth, quiet, but acoustically transparent flow surface. The volume behind this flow surface is filled with 0.457m-high foam wedges designed to eliminate any acoustic reflections at frequencies above 190Hz. The lower wall of the test section has the same construction except in the area immediately around the model mount where solid walls are used. The partial side walls (figure 1) include 150-mm deep acoustic absorbers filled with a combination of melamine foam and fiberglass insulation and covered with a tensioned Kevlar flow surface. The upper and lower walls contain hardware for the (vertical) mounting of two dimensional airfoil models. Models are rotated to angle of attack about their ¼-chord location centered midway between the acoustic windows and 3.6m from the upstream end of the test section. Models completely span the vertical height of the test section.

Plain weave Kevlar 120® cloth (58grams/m^2) is used to form the acoustic windows. The cloth is stretched on 5.37x2.51m tensioning frames. The Kevlar windows are sewn from 3 lengths of Kevlar cloth. When mounted, the two 40mm-wide seams run streamwise along the test section 0.19 to 0.28m below the upper wall and a similar distance above the lower wall.

Two anechoic chambers are positioned on either side of the test section. Each chamber has a streamwise length of 6m, extends 2.8m out from the test section acoustic window, and has a height of 4.2m. The chamber walls are constructed from medium density fiberboard, supported by a network of external steel beams, and lined internally with 0.610-m high acoustic foam wedges. Quarter-elliptical foam sections surround the acoustic windows so as to form a smooth transition between the lower and upper walls of the test section, on the inside of the windows, and the acoustically treated walls of the anechoic chambers on the outside of the acoustic windows.

B. Tension of the Kevlar windows.

The Kevlar material forming the acoustic windows is mounted on large tensioning frames that are, in turn, bolted to the structure of the test section. The total tension in each Kevlar window is partly generated by the tensioning frame, and partly by the support of the frame by the test section. The tension influences, to a limited extent, the small deflections of the Kevlar windows that are produced under aerodynamic load, such as when a lifting model is placed in the test section.

The tension of the acoustic windows was measured using a Newman ST-Meter 2E tension meter. While the meter is designed to measure the tension of a horizontally oriented membrane it was found to be useable on the vertically mounted acoustic windows as long as the meter was only pressed lightly to the window and didn't cause significant deflection. Measurements indicated a tension at the center of the windows of 1550N/m and 1400N/m for the port and starboard side respectively.

C. Porosity of the Kevlar cloth.

The Kevlar 120 scrim is not impermeable, but has about a 6% open area ratio. Thus local pressure differences across the Kevlar windows can induce local flow through them. We are therefore interested in the relationship between pressure difference across the Kevlar scrim and the velocity of the flow through it, since this forms one of the test section boundary conditions. A Kevlar sample was stretched across the mouth of a PVC pipe over which was fitted a flexible duct delivering air from a variable speed fan. The pipe was mounted with its open end, and the Kevlar sample, flush with the test wall of a small wind tunnel. With the wind tunnel on, the flow tangent to the Kevlar sample consisted of a free stream of 25m/s and a boundary layer some 25mm thick. Flow rate through the Kevlar (and thus the average transpiration velocity through it V) was measured as a function of the pressure difference across it Δp. Measurements were made with and without the wind tunnel flow, and with both directions of flow through the Kevlar. Regardless of the presence of the wind tunnel flow, or the direction of the flow through the Kevlar, the relationship between the velocity and pressure can be closely modeled by an equation of the form

$$\frac{V}{U_\tau} = E\left(\frac{\Delta p}{\frac{1}{2}\rho U_\tau^2}\right)^n \tag{1}$$

Here E and n are dimensionless constants, found to be 0.0176 and 0.5734 respectively, and U_τ is the viscous scaling velocity ν/L, with ν being the kinematic viscosity and L the average pore width in the Kevlar (measured as 3.53×10^{-4} m). As a practical matter, the constants in equation 1 were actually determined by fitting the simpler relation

$$V = C\Delta p^n \tag{2}$$

to the experimental data, where the dimensional constant $C = EU_\tau / (\frac{1}{2}\rho U_\tau^2)^n$ was found to be 0.03879, in SI units. The value of E was then determined using typical local conditions (ν=1.66×10^{-5} m^2/s, ρ=1.10 kg/m^3).

D. Airfoil models

Wind tunnel tests were performed on three airfoil models: a 0.91-m chord airfoil with DU97-W-300 section, a 0.91-m chord NACA 0012 airfoil and a 0.61-m chord NACA 0015 airfoil. The 30% thick highly cambered DU97 section is in marked contrast to the slim uncambered form of the NACA 0012 (figure 2). The DU97 and NACA 0012 models, constructed by Novakinetics LLC, were designed to span the complete vertical height of the test section. They are built around 88.9-mm diameter steel tube that forms a spar centered on the quarter chord location. The models have a fiberglass composite skin and a fill of fiberboard and polyurethane foam. These models were instrumented with about 80 pressure taps of 0.5mm internal diameter located near the midspan. The NACA 0015 was made from aluminum as an extruded section. It was instrumented with 48 pressure taps arranged in a single chordwise row close to center span.

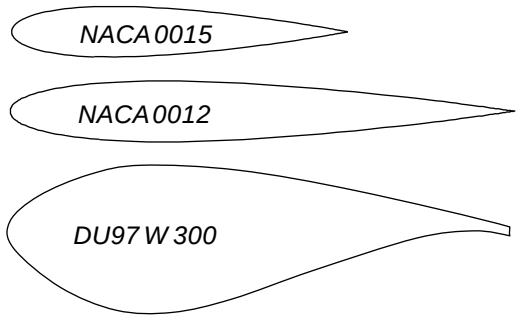

Figure 2. *Scale comparison of airfoil section shapes and sizes.*

Some measurements with the NACA 0015 and NACA 0012 airfoils were made with a serrated trip tape (Glasfaser-Flugzeug-Service GmbH 3D Turbulator Tape) applied with its leading edge at the 10% chord location on both sides of the airfoil. The tape has a thickness of 0.5mm and is 12mm in overall width. The leading and trailing edges are cut to form aligned serrated edges with a 6mm distance between points.

For some measurements boundary layer fences were attached near the ends of the DU97 and NACA 0015 airfoil models. Measurements made with and without fences were compared to reveal the importance of end effects on the airfoil flows. The fences consisted of 6-mm thick aluminum plates cut with an inner boundary matching the shape of the airfoil profile, and an elliptical outer boundary with its major axis forming an extension of the airfoil chord line. For the DU97 airfoil the major and minor axes of the ellipse were 1100mm and 394mm, with the ellipse protruding 100m forward of the leading edge and with an angle of 0.8^o between the ellipse axis and the airfoil chordline in the direction of positive angle of attack. For the NACA 0015 airfoil these numbers are 711, 194 and 50mm, and 0^o respectively. For both airfoils the fences were placed 235mm inboard of the ends of the models.

III. Aerodynamic Measurements

Mean surface pressure distributions on the airfoil models were measured over a range of conditions using an Esterline 9816/98RK pressure scanner with ranges of ±10 inches of water column and ±2.5psi. The system has a rated accuracy of ±0.05% full scale. Measurements with the DU97 were made at a chord Reynolds number (Re) of 1.875 million and geometric angles of attack α of 0, 6.7 and 13.2 degrees, with no boundary layer trip. Measurements with the NACA 0015 airfoil were made at a broad range of conditions including (a) Re=1.25 million, α=-20 to 20 degrees angle of attack (1 degree steps or less), both tripped and untripped, and (b) Re=0.35 to 2.65 million (in steps of 0.5 million or less), α=0, 6.75, 11.75 degrees, untripped. Measurements with the NACA 0012 airfoil were made at a similarly diverse set of conditions including Re=1.52, 2.26 and 2.87 million, α=-12, -9, -6, -3, 0, 3, 6, 9, 12 degrees both with and without trip. Selected pressure distributions will be presented in section V in comparison with viscous free-flight calculations and predictions of aerodynamic interference effects.

All of the above measurements were made without boundary layer fences installed on the models. However, for selected conditions, pressure measurements on the DU97 and NACA 0015 airfoils were made with the fences installed. Furthermore, at representative conditions with these models, tuft flow visualizations were performed on the inside surfaces of the acoustic windows using tufts made from Nylon yarn. The tufts were placed in a square grid pattern with a separation of about 30cm over the whole surface of each window. The tuft flow visualizations showed flow in the test section to be well behaved and attached to the Kevlar acoustic windows at all conditions (including the largest airfoil, the DU97, at the greatest angle of attack). Furthermore, airfoil pressure distributions were found not to be measurably influenced by the fences placed near their spanwise ends, suggesting that end effects, such as contamination of the airfoil flows from the test section boundary layers, were not significant. One exception here was the DU97 model, for which the fences showed no effect except (ironically) to trigger early stall at 13.2 degrees angle of attack.

IV. Aerodynamic Modeling and Corrections

Calculations were made to model the effects of the wind tunnel walls on the airfoil aerodynamics using a hybrid panel method extended to account for presence of the wind tunnel walls and acoustic windows, the transpiration of air into or out of the test section through the windows, and the deflection of those windows under aerodynamic load. In addition, a theoretical model has been developed to provide a correction formula for the associated lift interference. Calculations and corrections have been compared with representative experimental results.

A. Panel method model

A standard linear vortex panel scheme was used to model flow around the airfoils. The scheme was used by itself to compute the free-flight aerodynamics of the airfoils (for comparison), and as part of the hybrid interference method. The design shapes of the airfoils were each discretized into some 200 straight vortex panels of linearly varying strength. A control point was placed at the center of each panel. The panel strengths were inferred by requiring that the non-penetration condition be satisfied at each of the control points and that the Kutta condition be satisfied at the trailing edge. The finite trailing edge thickness of the DU97 was handled by placing a source panel of constant strength across the blunt base. The panel method was validated by comparison with inviscid calculations performed using the well known Xfoil code (Drela, 2009).

The basic airfoil calculation method described above was extended to model the wind tunnel interference by including a series of constant-strength source panels arranged along the side-walls of the test section. A total of 98 panels were used to represent each wall extending 20.4m upstream and downstream of the airfoil ¼-chord location (compared to the test section width of 1.85m). Minimum panel length (near the airfoil) was 0.06m, while the maximum was 0.62m furthest from the airfoil. Control points were placed at the center of each panel. By enforcing the non-penetration at the control points and solving for the panel strengths simultaneously with the airfoil solution described above, the code simulates the blockage effects of a solid wall test section.

The actual test section walls do not, of course, behave as perfect solid walls over the 5.14m length of the acoustic windows. Here pressures on the windows, set up by the airfoil flow, cause air to be drawn into or driven out of the test section into the anechoic chambers. Modeling the presence of this transpiration in the panel method is a straightforward modification of the boundary condition applied at the control points of the panels representing the acoustic windows. Instead of requiring that the velocity component perpendicular to the wall is zero at these points, it is set to be equal to the transpiration velocity into or out of the anechoic chamber. The problem of course is determining the transpiration velocity, and this can be done using the velocity pressure difference relation for the Kevlar scrim given in section II.C. The pressure difference across the Kevlar is given by the pressure calculated in the panel method at the inside of the acoustic window, and an

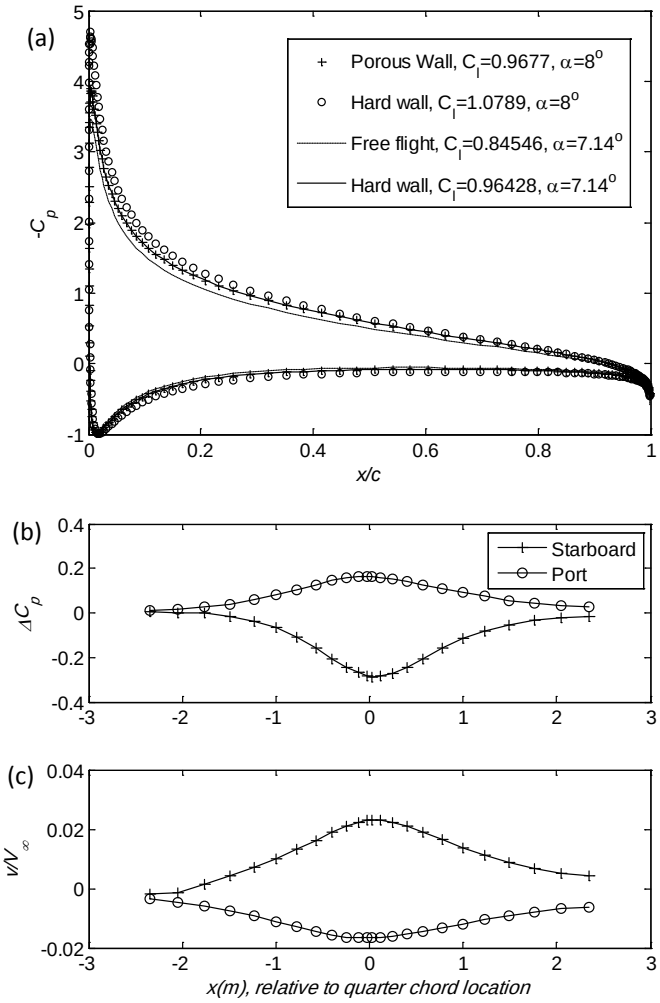

Figure 3. *Results of calculations using the hybrid panel method with porous walls for the NACA 0012 airfoil at 8 degrees angle of attack. (a) Pressure distribution compared with calculations for free flight and an equivalent hard-wall test section (b) distributions of pressure and (c) transpiration velocity along the length of the acoustic windows.*

estimate of the pressure in the anechoic chambers. This pressure can be estimated by requiring that no net mass flow exit the test section through the acoustic windows. Since the pressure difference relation is non-linear, this porous wall boundary condition must be satisfied by iteratively adjusting the pressure in the anechoic chambers and re-computing the flow until the mass flow condition is satisfied.

Results of a sample calculation are shown in Figure 3 for the 0.91-m chord NACA 0012 at 8 degrees angle of attack in terms of pressure distributions on the airfoil, pressure distributions on the Kevlar windows and transpiration velocities through the windows. The effect of the porosity is, primarily, to reduce the magnitude of the pressure coefficient on the suction side of the airfoil (Figure 3a). Transpiration through the Kevlar is greatest near the quarter chord location of the airfoil (x=0, figure 3b). Velocities are greatest into the test section on the starboard (suction) side of the airfoil, and peak at 2 to 3% of the free stream speed. Transpiration velocities reduce towards the ends of the windows and are distributed in a qualitatively similar manner to the pressure.

The changes in the airfoil pressure distributions due to the porosity of the Kevlar and the different mass flow conditions are almost identical to those that would be produced by a change in angle of attack, as shown in figure 3a. With porosity the airfoil flow is almost identical to that which would be produced in the solid wall test section at an angle of 7.14^o. This observation is important. It implies that the Kevlar walls are in the 'aerodynamic farfield' and that the effects of their porosity can be corrected for simply by adjusting the angle of attack. Note that the pressure distribution for the airfoil computed in the solid-wall test section is still slightly different from the free flight prediction, implying a non-negligible blockage correction. However, as will be discussed further below very little blockage correction is realized in practice with the Kevlar walls.

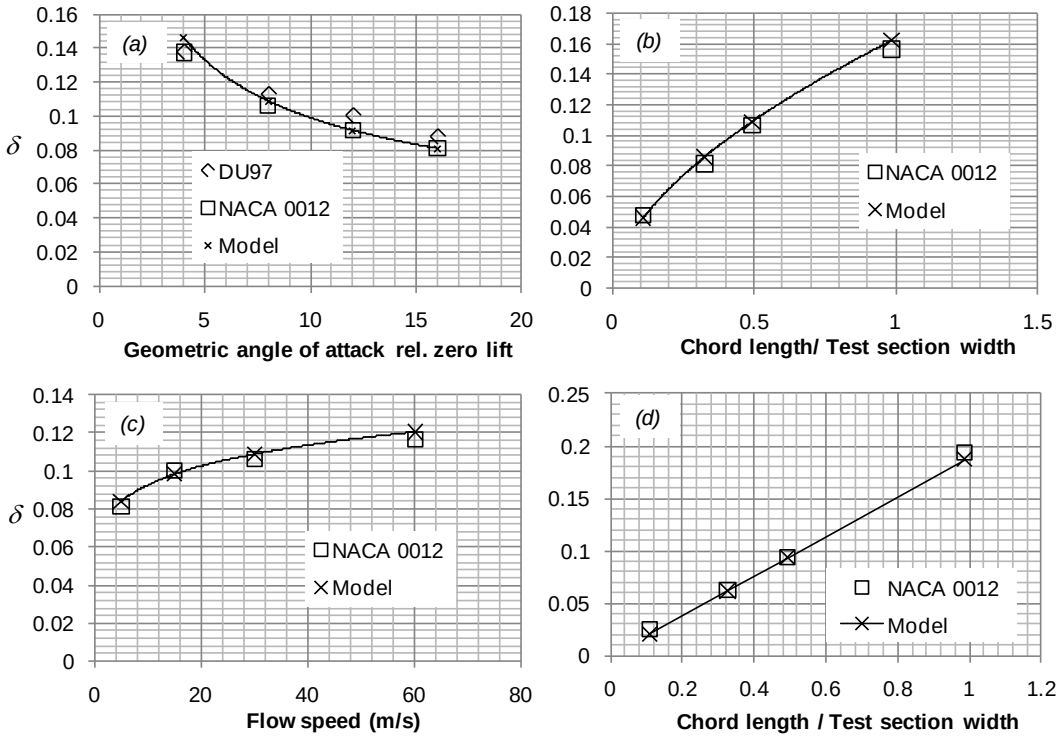

Figure 4. *Effects of different parameters on the proportionate angle of attack correction to hardwall δ as computed using the hybrid panel method (squares and diamonds) and using equation 10 (lines and crosses). (a) Effect of airfoil shape and angle of attack (b) Effect of airfoil size, (c) effect of flow speed, and (d) effects of chordlength with a hypothetical linear porosity relation for the Kevlar cloth.*

B. A simplified model for angle of attack corrections

A series of panel method calculations were performed using the porous test section wall model for different angles of attack, airfoil shapes and chordlengths to reveal the broader effects of porosity on the aerodynamics. In all cases, the effects of the porosity on the airfoil pressure distributions were found to be almost indistinguishable from the effects of an angle of attack change. We therefore define the proportionate angle of attack correction δ as,

$$\delta = \frac{\alpha_g - \alpha_e}{\alpha_g - \alpha_{0l}} \tag{3}$$

where α_g is the geometric angle of attack, α_e is the observed effective angle of attack and α_{0l} is the zero lift angle of attack of the airfoil section. That is, the effective angle of attack is given by

$$\alpha_e = \alpha_g - (\alpha_g - \alpha_{0l})\delta \tag{4}$$

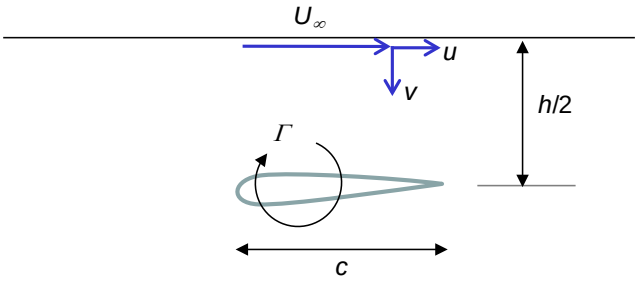

Figure 5. *Schematic showing variables used in the derivation of the porosity correction formula.*

Sets of calculations were performed to determine the dependence of the effective angle of attack correction δ first on angle of attack (figure 4a) for the DU97 and NACA 0012 airfoils. The chord to test section width ratio for these airfoils is h/c=0.493. The proportionate angle of attack correction is not constant but reduces by almost 40% as the angle of attack increases from 4 to 16 degrees. It is, however, almost identical for the two airfoils making it unlikely that it is a function of airfoil shape. Figure 4b shows the effect of chordlength (in terms of h/c) for the NACA 0012 at 8 degrees angle of attack. Increasing the chordlength increases δ but following a non-linear variation. Figure 4c shows the effect of flow speed on the correction for a 0.91-m chord NACA 0012 at 8 degrees angle of attack. There is an effect of speed (a gradual increase in the correction) because the exponent in the porosity relation (see section 2.3), is not exactly 0.5 implying some Reynolds number dependence. Figures 4d shows again the effects of chordlength on the NACA 0012 but with the porosity relation replaced by a hypothetical linear expression between velocity and pressure. Interestingly, this results in a linear dependence of the correction with chordlength, as opposed to the non-linear dependence seen in figure 4b. This is an important clue for the development of a simplified relation for the effects of the porosity, since it implies an intimate relationship between the correction and the porosity relation.

Consider the airfoil between porous walls, as illustrated in figure 5. The airfoil generates a circulation Γ and this circulation acts to increase or decrease the velocity along the porous walls near the airfoil. The maximum change will be $\Gamma/\pi h$, felt immediately above or below the quarter chord. The actual deviation from the free stream velocity on the walls will have a typical value that is reduced from this number, since it would represent the average over some streamwise distance, but then increased by the effects of the images of the airfoil in the tunnel walls. We therefore write this typical value as

$$u \approx A\frac{\Gamma}{\pi h} \tag{5}$$

where A is a constant, expected to be of order 1. In terms of the lift coefficient on the airfoil C_l this expression is,

$$u \approx A\frac{C_l U_\infty c}{2\pi h} \tag{6}$$

This velocity deviation results in a non-zero pressure coefficient on the acoustic window with a magnitude of

$$|C_p| \approx \frac{2u}{U_\infty} \approx A\frac{|C_l|}{\pi}\frac{c}{h} \tag{7}$$

where we have used the linearized form of the pressure coefficient.

The pressure acting on the porous walls is what draws the flow through them, resulting in a transpiration velocity with a magnitude given by a relation of the form,

$$|v| = C|\Delta p|^n \tag{8}$$

(such as in section II.C) where Δp is the difference between the pressure on the acoustic window and the pressure in the chamber behind it. If we assume the chamber pressure is only slightly different than the free stream pressure (a good approximation), then this expression can be re-written as,

$$\frac{|v|}{U_\infty} = \frac{C}{U_\infty}(\tfrac{1}{2}\rho U_\infty^2)^n |C_p|^n \tag{9}$$

Now, v/U_∞ is the typical flow angle at the wall that results from the porosity. We would therefore expect this to also be the reduction in the effective angle of attack that results from the porosity. Substituting equation 7 for the pressure coefficient, we therefore have, in radians

$$\alpha_g - \alpha_e \approx \frac{v}{U_\infty} \approx \mathrm{sgn}(C_l)\frac{C}{U_\infty}\left(\tfrac{1}{2}\rho U_\infty^2 \frac{|C_l|}{\pi}\frac{c}{h}A\right)^n \tag{10}$$

or

$$\delta \approx \frac{\mathrm{sgn}(C_l)}{\alpha_g - \alpha_{0l}}\frac{C}{U_\infty}\left(\tfrac{1}{2}\rho U_\infty^2 \frac{|C_l|}{\pi}\frac{c}{h}A\right)^n \tag{11}$$

Qualitatively this expression matches the behavior observed in figure 4. For the porosity relation given in section 2.3 (n=0.5734), the normalized correction should decrease with angle of attack (figure 4a), increase with chordlength (figures 4b) and velocity (figure 4c). For the linear porosity relation (n=1) the increase with chordlength should be linear (figure 4d). We also note that in the limit of high Reynolds number flow through the porous walls (for which we would expect n=0.5), the correction should become independent of velocity, as would be expected.

Quantitative results calculated using this expression are included in figure 4. Note that for the DU97 a zero lift angle of attack of -2.35 degrees was used. The constant A was simply set to 1 and thus, and in that sense these represent absolute predictions. The agreement for the variations in chordlength, angle of attack and velocity is quite good. The method also accurately predicts the level of the linear variation in figure 4d, suggesting that the influence of the porosity relation is correctly captured in this expression.

C. Comparison between measurements and predictions

In this section the results of interference calculations performed with the above methods are compared with representative experimental results from section 3. Experimental results are also compared with free-flight viscous calculations performed using Xfoil (Drela, 2009). Interference calculations were performed using the measured conditions and the independently established porosity relation introduced in section II.C.

Figure 6 shows measured pressure distributions for the 0.61-m chord NACA 0015 airfoil for geometric angles of attack of 0, 6.75 and 11.93 degrees. The measurements shown were made without fences but, as discussed in chapter 3, these had no effect. The Reynolds number is 1.26×10^6. At zero angle of attack (figure 6a) the measurements agree closely with the free flight inviscid and viscous solutions. At 6.75 and 11.93 degrees (figures 6b and c) differences appear. This is partly because of the

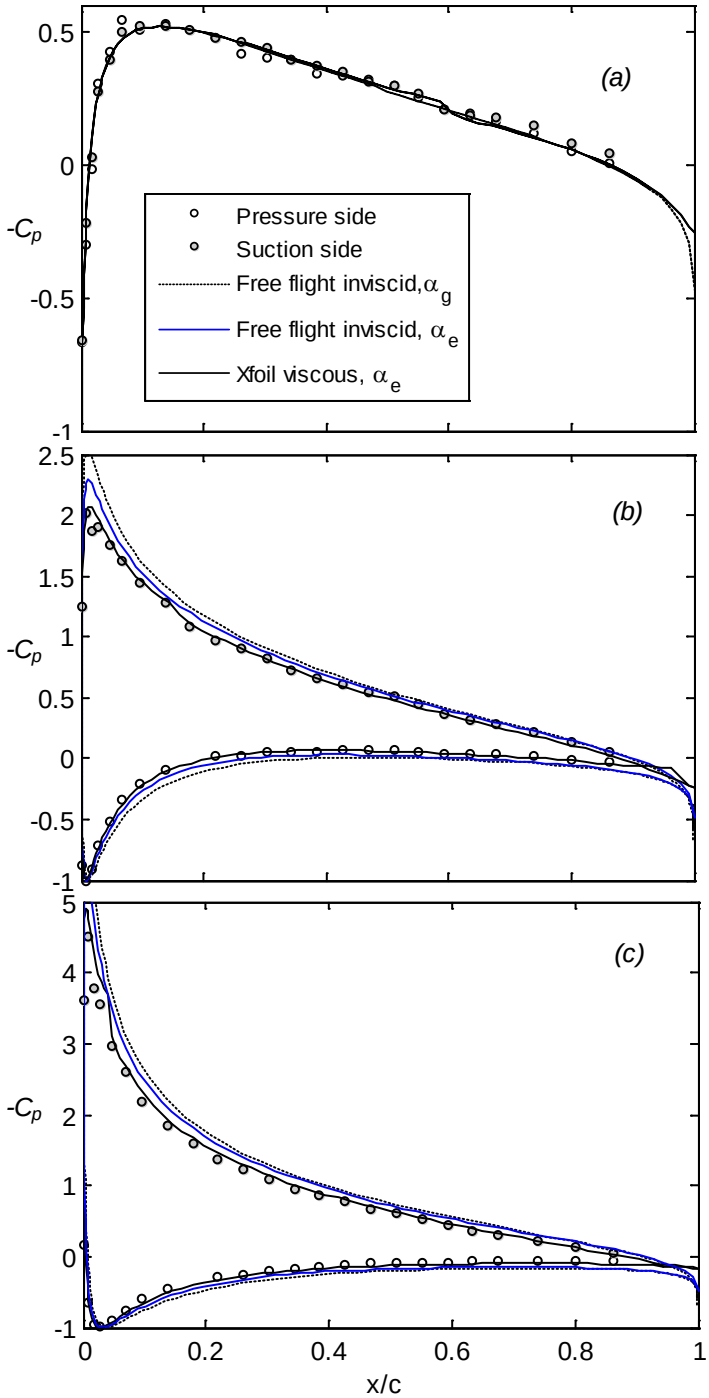

Figure 6. *Measured pressure distributions for the 0.61-m chord NACA 0015 airfoil for Re = 1.26×10^6. (a) $\alpha_g=\alpha_e=0^o$, (b) $\alpha_g=6.75^o$, $\alpha_e=6.12^o$ and, (c) $\alpha_g=11.93^o$, $\alpha_e=11.06^o$.*

test section interference and partly due to viscous effects. The effects of interference are apparent in smaller peak pressures on the suction side. This is a result of the porosity of the acoustic windows and the change in effective angle of attack it produces. Predicting the effective angle of attack using equation 11 (with constant A=1) gives 6.12 and 11.06 degrees for these two cases, and viscous free flight calculations at these angles of attack agree closely with measurements. Interestingly, the comparison of the viscous and inviscid free-flight calculations shows a non-negligible viscous effect. Note that these corrections are many times smaller than those which would be needed for an equivalent open-jet test-section configuration.

Good agreement was also observed between the measurements and Xfoil calculations for all other measured conditions when the effective angle of attack of the airfoil predicted by equation 11 was used for the Xfoil calculation. While the individual pressure distributions are too numerous to show here, some of them are summarized in Figure 7 in terms of the sectional lift and moment coefficients integrated from the pressure distributions. Differences between the measured and computed coefficients (at the effective angle of attack) are small everywhere except beyond about 10 degrees angle of attack where stall becomes significant and the Xfoil calculation would not be expected to be accurate. Figure 7 includes two sets of measurements made some 3 months apart and separated by a complete disassembly and reassembly of the entire anechoic system. The agreement between these measurements is thus a measure of the repeatability of the aerodynamic characteristics of the test section and the consistency of the interference correction.

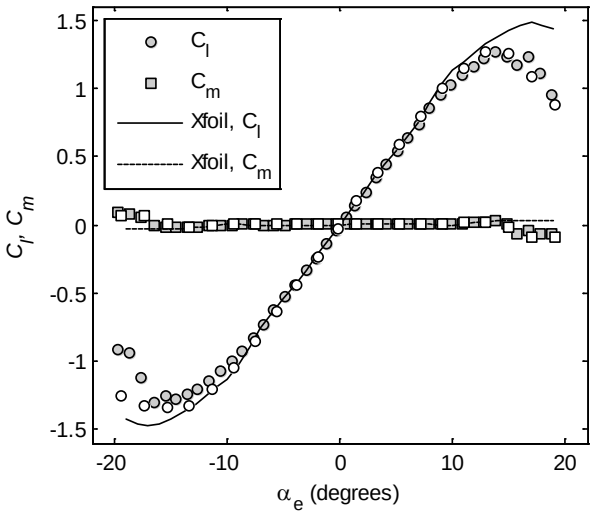

Figure 7. *Lift and moment coefficients for the NACA 0015 airfoil, obtained by integrating measured pressures, and Xfoil viscous predictions (untripped, $Re=1.26\times10^6$). Data shown with white symbols measured 3 months after data with gray symbols.*

Figure 8 shows some representative comparisons between mean pressure distributions measured on the 0.91-m chord NACA 0012 airfoil, and Xfoil predictions at the *a priori* effective angle of attack determined from equation 11. The cases shown here are for a Reynolds number of 2.9 million. A more extensive sample of comparisons are summarized in figure 9 in terms of integrated lift and moment coefficients for a range of angles of attack at different Reynolds number and trip combinations. In all cases the agreement appears very satisfactory.

Figure 10 compares mean pressures measured on the 0.91-m chord DU97 at 0, 6.67 and 13.2 degrees angle of attack, and a Reynolds number of 1.88 million, with calculations made using the Xfoil at the effective angle of attack. While not quite as close as the match for the NACA profiles, the agreements between the measurements and Xfoil remains good, with the largest differences appearing over the last 20% chord where measured pressure coefficients are about 0.15 in C_p lower than the free-flight calculation. Small differences are also apparent near the leading edge at 13.2 degrees (figure 10c) and on the suction side at zero angle of attack (figure 10a).

D. The Blockage Effect

One remarkable aspect of the measurements presented in the previous sections is that they appear to display almost no effects of test section blockage. This is unexpected: these are not small airfoil models and calculations performed to reveal the influence of the test section walls upon their aerodynamics do suggest that blockage effects should be significant, if not substantial. This is particularly true for the DU97 airfoil which, even at zero angle of attack, has a forward projected area equal to 15% of the cross-sectional area of the test section. Figure 10 includes pressure distributions (dashed lines) calculated using the panel method, which should account not just for the porosity of the Kevlar (and thus the effective angle of attack) but also the confining effects of the walls. The calculations at 6.67 and 13.2 degrees show a large blockage effect, particularly on the suction side of the airfoil, where pressures are as much as $1.0C_p$ lower than those indicated by the free-flight calculation.

An obvious explanation might be that the Kevlar walls are not only porous but also flexible. To account for flexibility the panel method was extended to model the Kevlar sidewalls as membranes under tension, the deflection being solved for simultaneously with the aerodynamics and the porosity. Computed deflections turn out to be quite

realistic, but the computed airfoil pressure distributions are no closer to the measurements, as shown in figure 10 for the DU97.

While the physical cause of the weak influence of the test section walls on these airfoil flows remains under study, the small residual differences between the measurements and the free-flight X-foil calculations can be accounted for using a modification to the traditional blockage correction.

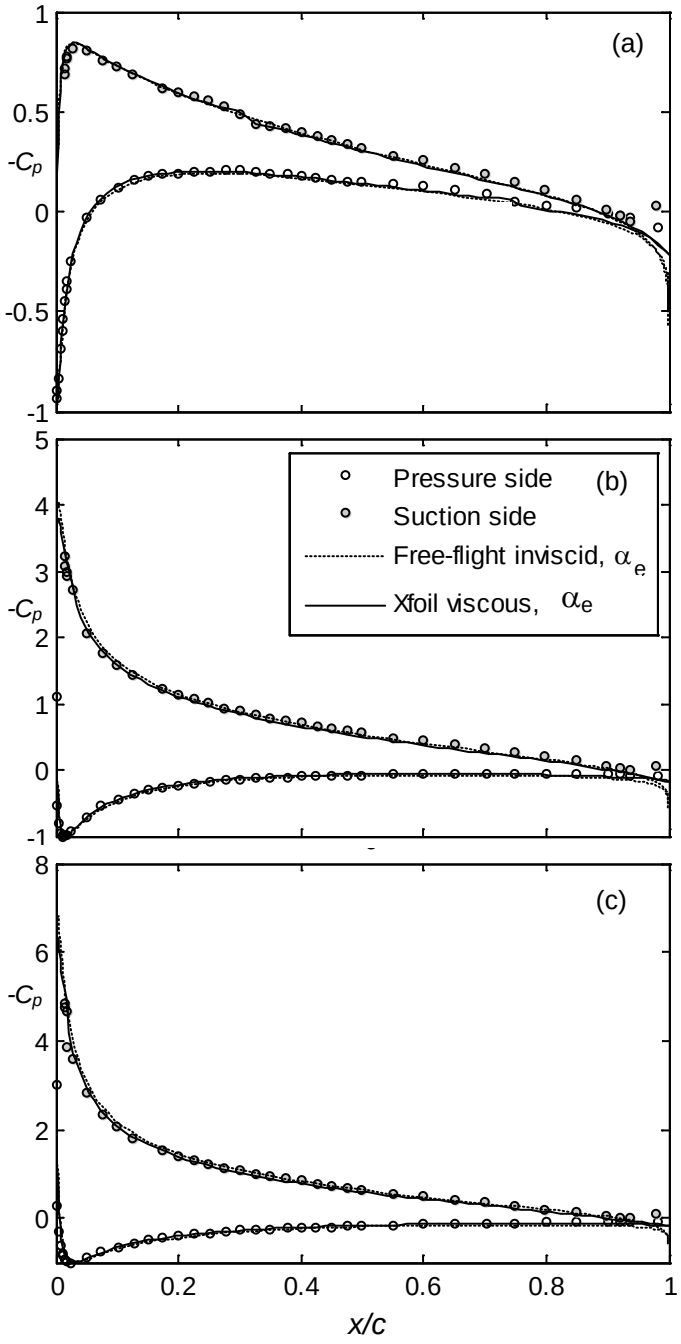

Figure 8. *Sample comparisons between measured and predicted pressure distributions for the untripped NACA 0012 airfoil at Re=2.85×10^6. (a) α_g=3.02^o, α_e=2.28^o, (b) α_g=8.99^o, α_e=7.79^o, (c) α_g=12.03^o, α_e=10.65^o.*

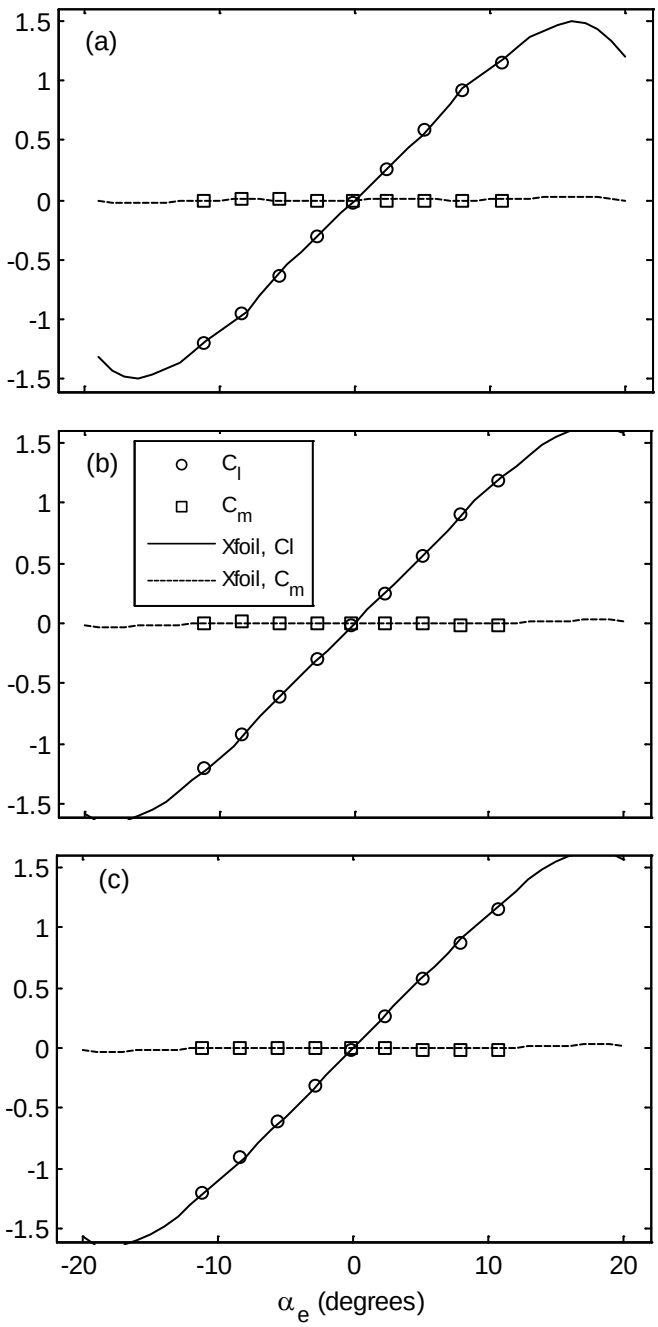

Figure 9. *Lift and moment coefficients for the NACA 0012 airfoil, obtained by integrating measured pressures, and Xfoil viscous predictions.(a) Re=1.52×10^6, untripped, (b) Re=2.87×10^6, untripped, and (c) Re=2.87×10^6, tripped.*

This approach is examined by performing Computational Fluid Dynamics (CFD) calculations for the DU97 airfoil in free flight, and comparing the results to the wind tunnel data corrected using a modified form of a classical blockage correction. The modification is an *ad hoc* adjustment of the blockage magnitude. This approach verifies that a blockage mechanism very similar to solid wall blockage, albeit at reduced magnitude, is present for very thick models.

The CFD computations described in this section were performed using the SACCARA Reynolds-Averaged Navier-Stokes (RANS) code (Wong *et al.*, 1994), a structured-mesh finite volume compressible flow code developed at Sandia National Laboratories that has been extensively validated for external and internal aerodynamics problems. The Spalart-Allmaras turbulence model was used, and the Xfoil code was used to estimate boundary layer transition locations for free-transition cases. All computations were performed on a two-dimensional domain using structured, curvilinear meshes. A very fine computational mesh, with 490,000 total cells with wall-normal mesh spacing of $y+ < 1$, was used to ensure numerically converged results.

The solid wall interference corrections (Allen and Vincente, 1947) derive from thin airfoil theory. The corrections result from comparison of series solutions for the distribution of vorticity along the airfoil for both the free air and bounded flow cases. Matching of the two solutions is performed under the constraint that the magnitude of the suction peak of the corrected pressure distribution matches that of the free air pressure distribution. The results include formulas for corrected force coefficients, as well as a procedure for correcting the airfoil surface pressure distribution. Note that the pressure distribution correction is not simply a constant factor but, in general, provides a non-uniform adjustment of the distribution along the entire airfoil chord. The solid wall corrections include the effects of both solid blockage and of streamline curvature. The streamline curvature effect results in an additional correction to the angle of attack. Details of the corrections and underlying theory may be found in Allen and Vicente (1947). The resulting solid wall free stream velocity increment due to blockage is (for incompressible flow)

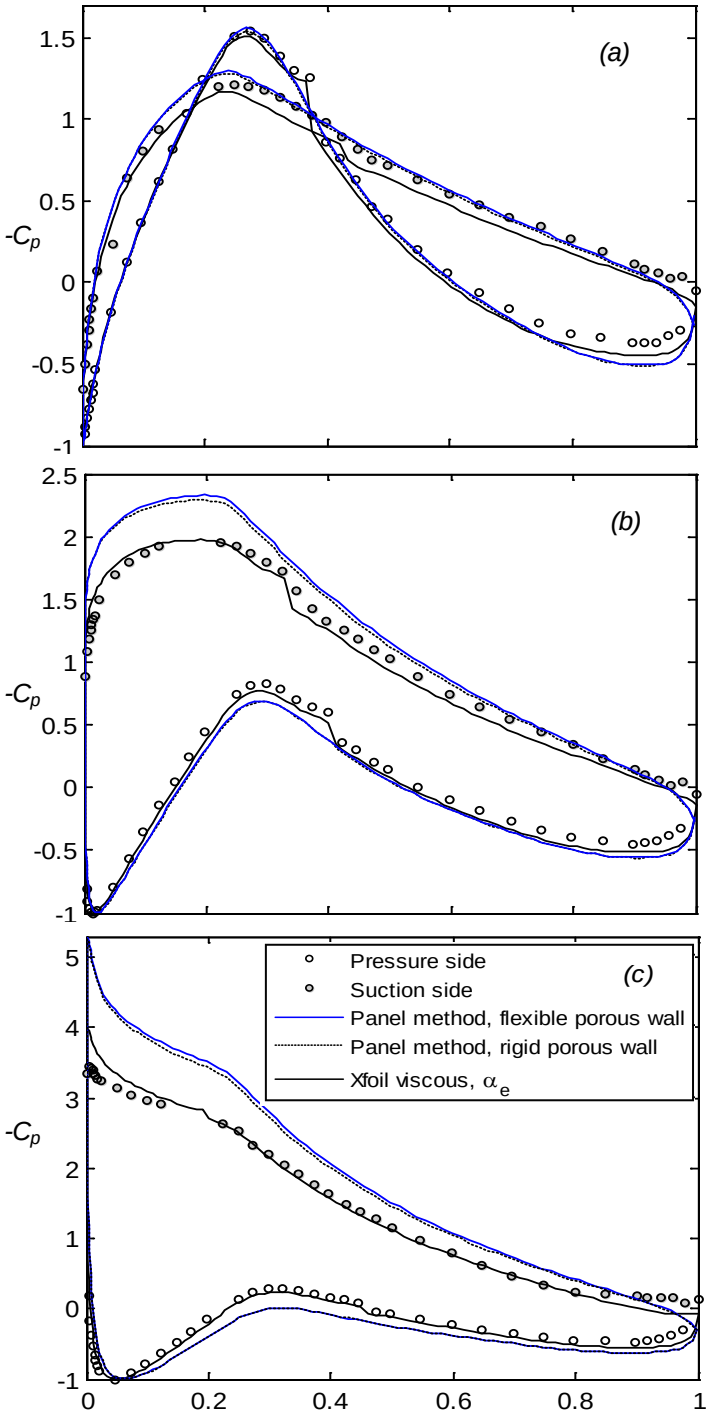

Figure 10. *Measured and predicted pressure distributions for the DU97 W300 airfoil at Re=1.88×10^6. (a) $\alpha_g=0^o$, $\alpha_e=-0.43^o$, (b) $\alpha_g=6.67^o$, $\alpha_e=5.74^o$, (c) $\alpha_g=13.2^o$, $\alpha_e=11.93^o$.*

$$\frac{u'_{sw}}{U_\infty} = \Lambda\sigma \qquad (12)$$

where the parameter Λ depends on the symmetric component of the airfoil shape, and with

$$\sigma = \frac{\pi^2}{48}\left(\frac{c}{h}\right)^2 \tag{13}$$

In order to assess the applicability of the solid wall blockage correction method to the surface pressure distribution over the DU97, a numerical experiment was performed. First, the pressure distribution was computed using CFD for the airfoil with solid side wall boundaries at an angle of attack of 5.74 degrees and *c/h = 0.5*. The side walls were modeled as free-slip boundaries, with the assumption that the side wall boundary layers would have only a small effect on the blockage. Next, the pressure distribution was computed for free-flight conditions at an angle of attack of 6.00 degrees, which corresponds to the effective angle of attack including the solid wall streamline curvature effect (see Allen and Vicente (1947)). The solid wall blockage corrections were then applied to the in-tunnel computational results. Comparison of the two cases is shown in Figure 11. The maximum difference in C_p between the corrected and free-flight distributions is about 0.04. This level of agreement verifies the blockage correction method for the present airfoil with solid wall test conditions.

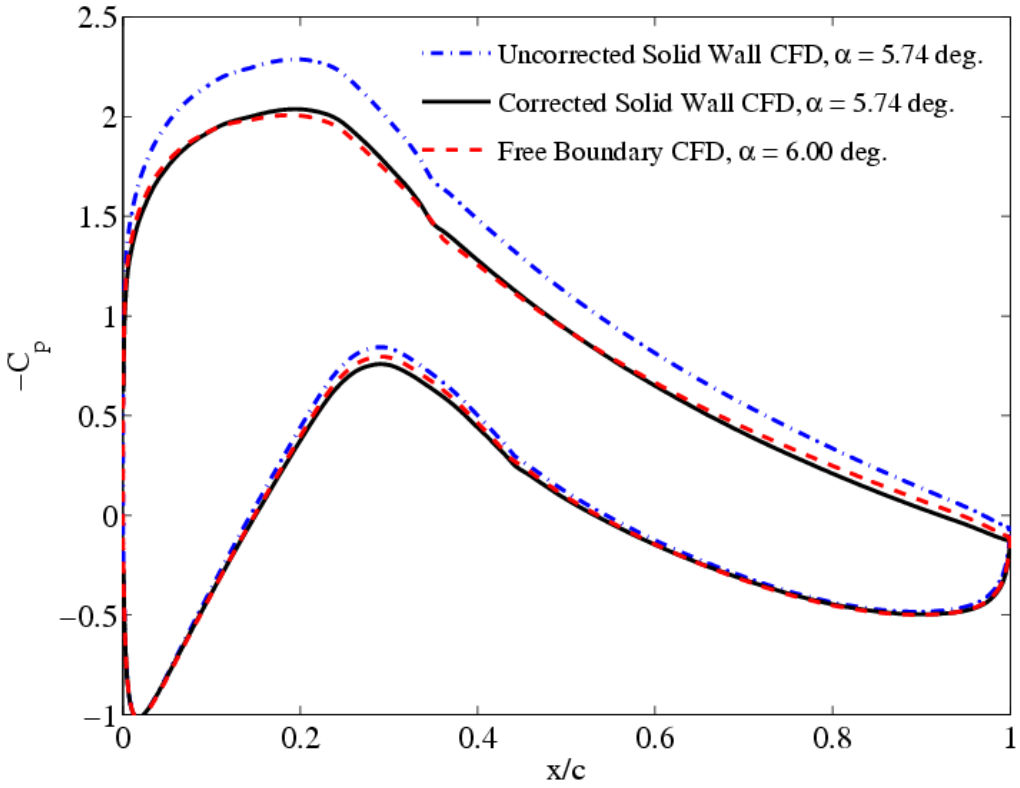

Figure 11. *Comparison of free-flight and corrected solid wall CFD surface pressure distributions for the DU97 airfoil.*

It remains to assess the blockage for the porous wall. One approach for treating porous test section blockage is to introduce a factor Ω relating the porous wall blockage to solid wall blockage such that

$$\frac{u'_{pw}}{U_\infty} = \Omega \frac{u'_{sw}}{U_\infty}. \tag{14}$$

The value of Ω has previously been calculated (Ewald, 1998) for a range of porous wall resistances for two-dimensional test sections, assuming a linear relationship between transpiration velocity and pressure differential across the walls. For the present configuration, the empirically derived wall boundary condition is nonlinear (see section II.C). Further, application of the empirical boundary condition overestimates the blockage effect, as discussed earlier. Given this situation, we simply hypothesize that a value for Ω exists that corrects for the slight amount of blockage observed in the DU97 pressure distributions.

This hypothesis is tested by comparing free-flight CFD results for the DU97 with corrected pressure distributions at the three measured effective angles of attack. The effective angle of attack is determined solely from the porous wall downwash correction derived in Section III.B; any influence of streamline curvature is assumed to be included

in this correction. Two CFD solutions were obtained for each angle of attack: one with free boundary layer transition on both suction and pressure surfaces, and one with suction surface boundary layer transition location fixed at the leading edge and free transition on the pressure surface. The corrected pressure distributions apply a modification of the method of Allen and Vincenti (1947), where a value of Ω is chosen to give the best level of agreement with the free-flight CFD results at the intermediate angle of attack of 5.74 degrees. The degree of agreement was judged subjectively, and the best value of Ω was determined by a trial-and-error approach.

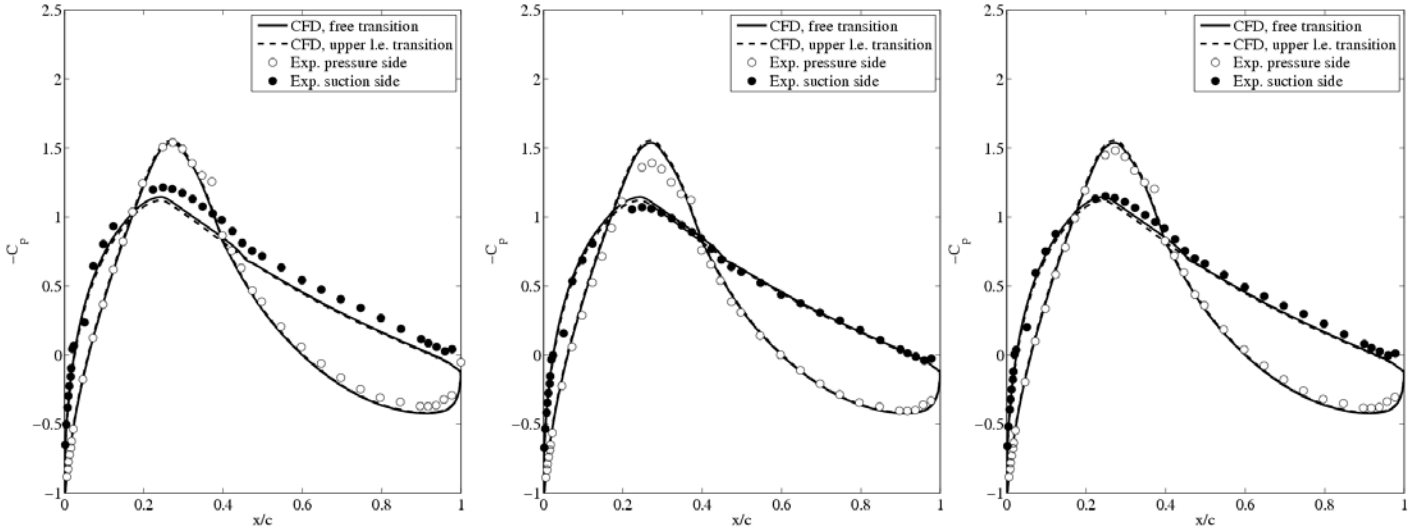

(a) Uncorrected. (b) Corrected, Ω = 1.0. (c) Corrected, Ω =0.42

Figure 12*. DU97 surface pressure distributions, a=-0.43 deg.*

Figure 12 shows three versions of the pressure distribution for α=-0.43 degrees: the uncorrected distribution, the distribution corrected for solid wall blockage (Ω=1.0), and the distribution corrected using the "best" value for porous wall blockage, Ω=0.42. These pressure distributions are compared to the free-flight CFD results. At this angle of attack, there is little difference between the free and fixed transition CFD results, and the CFD results also agree well with the Xfoil results presented earlier. The shape of the uncorrected pressure distribution show modest disagreement with the CFD results over the suction surface. Agreement improves over the suction surface with application of the full solid wall blockage correction, but agreement worsens over the pressure surface. The porous wall blockage correction with Ω=0.42 gives very good agreement over both the pressure and suction surface.

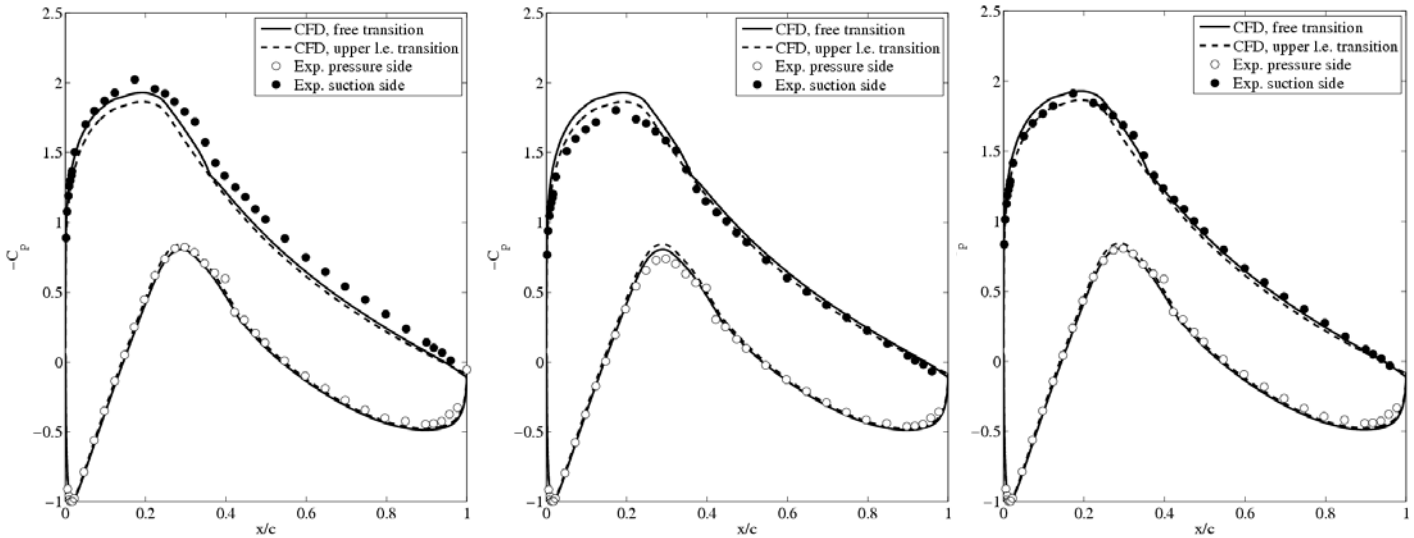

(a) Uncorrected. (b) Corrected, Ω = 1.0. (c) Corrected, Ω =0.42

Figure 13*. DU97 surface pressure distributions, a=5.74 deg.*

Figure 13 compares the measured pressure distributions with free-flight CFD results for α=5.74 degrees. The leading edge transition condition results in a slightly lower predicted suction peak relative to the free transition result, although there is no means of determining which condition is most appropriate for this case. The uncorrected experimental data show lower suction surface pressures than the CFD results. Application of the full solid wall correction over-corrects the pressures relative to the CFD results, while the porous wall correction with Ω=0.42 again results in uniform improvement in agreement with the CFD results.

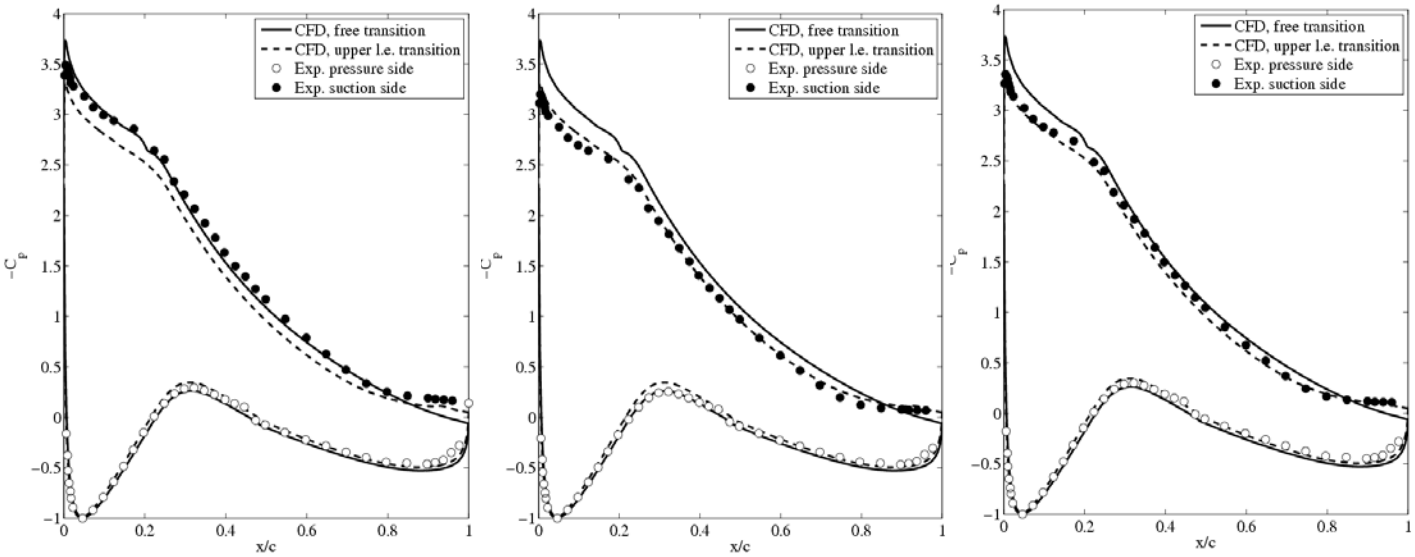

(a) Uncorrected. (b) Corrected, Ω = 1.0. (c) Corrected, Ω =0.42

Figure 14*. DU97 surface pressure distributions, a=-0.43 deg.*

For α=11.93 degrees (Figure 14), the measured pressure distributions indicate a region of separated flow on the suction surface near the trailing edge. The free-transition CFD solution, and the Xfoil solution shown previously, do not predict the full extent of this separation region, while the CFD solution with leading edge suction surface transition does. Clearly, correct prediction of the region of separated flow near the trailing edge is necessary for good prediction of the entire suction surface pressure distribution. The uncorrected measured suction peak lies in between that predicted by the free-transition and leading edge transition CFD cases. The full solid wall blockage corrections results in good agreement between the corrected pressures and the leading-edge transition CFD case, while the porous wall correction (again, with Ω=0.42) gives comparable agreement for the suction surface and a slight improvement for the pressure surface.

Overall, the comparisons with RANS CFD further confirm the porous wall angle of attack correction derived in Section IV.B. The shapes of the computed pressure distributions are close to the measured distributions, independent of any further blockage correction, and any further shift in angle of attack would not uniformly improve this agreement. The comparisons with CFD indicate that the full solid wall blockage correction is too strong, consistent with the panel code results, but that an ad hoc intermediate porous wall blockage correction gives improved agreement between computation and experiment. Further study is need to determine whether the porous wall blockage correction method with Ω=0.42 applies to other thick airfoils, and to understand the underlying reason for the difference between the observed blockage and the larger blockage predicted by the porous wall panel code method.

V. Acoustic Measurements and Modeling

This section describes the experimental tests carried out to determine the anechoic characteristics of the anechoic chambers and the acoustic losses due to propagation through the Kevlar and boundary layer.

A. Anechoic Chamber Characteristics

The first set of experiments was undertaken to determine the acoustic impedance and the resulting sound absorption/reflection of the anechoic chambers. Figure 15 shows the schematic of the experimental setup. A spherical speaker (Mod2 ORB Audio 3" diameter subwoofer, 28-20000 Hz frequency response) was positioned in the chamber facing the back wall of the anechoic chamber. A condenser type microphone (PCB Model 40AE with ICP preamplifier Model 426A02) was then positioned between the speaker and the wall and the transfer function between the speaker input and the microphone output signals measured. This measurement was repeated for 15 positions (distances from 4.25" to 60.25"). The speaker was driven with Pink Noise in the 0-1.6 KHz range. The data measured consisted of the transfer function (FRF), coherence, spectrum of the input signal to the speaker, and the spectrum of the microphone output signal. The microphone was calibrated using a B&K calibrator type 4231 (94 dB at 1000 Hz).

The magnitude of the transfer function for all positions was normalized to a distance of 1 meter using the far-field spherical spreading law (Bies and Hansen, 1988). Since it is in the geometric near-field of the speaker, the closest position of the microphone to the speaker was not included, *x=0.108 m (4.25")*. Figure 16 shows the normalized transfer function magnitudes showing that the data collapsed very well above 180 Hz. Thus, the cut-off frequency of the anechoic chamber is 180 Hz, e.g. acoustic absorption coefficient $\alpha = 1$ for *f*=180 Hz. On the other hand, the effect of the acoustic interference of the chamber walls is very clear below 100 Hz.

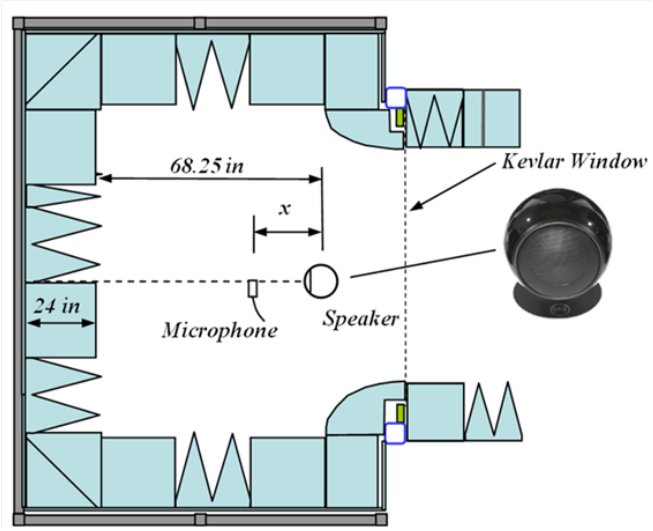

Figure 15. *Position of speaker and microphone to*

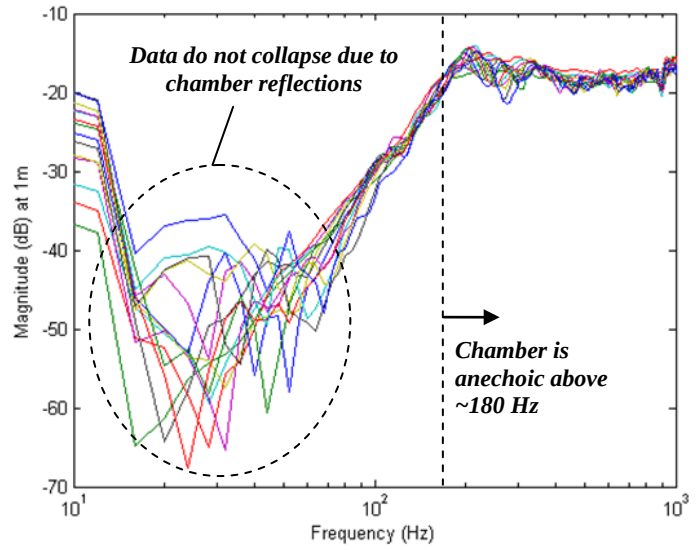

Figure 16. *Magnitude of transfer functions normalized to a distance of 1 meter.*

B. Kevlar and Boundary Layer Losses

This section describes the experimental procedure used to determine the sound propagation losses through the Kevlar walls and boundary layer used to correct the phased array results. These corrections were estimated in the past by Remillieux *et al.* (2008), using a pipe mounted in the test section and connected to a speaker driven with white noise, and also by Burdisso and Errasquin (2009) using a spherical shaped speaker located at the center of the test section. Since the effect of the flow on the radiation of such sources was a concern, a new approach was tested.

The tests consisted in driving with white noise a speaker located on the anechoic chamber opposite to the array (see Figure 17) and measuring the noise with the phased array for different flow speeds, including no flow such as to determine the Kevlar losses. By placing the speaker in the opposite anechoic chamber, and thus outside the test section, the radiation characteristics of the speaker were not affected by the flow around it. The losses were then determined by comparing the measurements to the sound level that the speaker would be producing without the presence of the Kevlar and flow, i.e. speaker radiating in free-field. The free field radiation data was obtained measuring the noise from the speaker located in the same chamber than the phased array, i.e. no losses configuration.

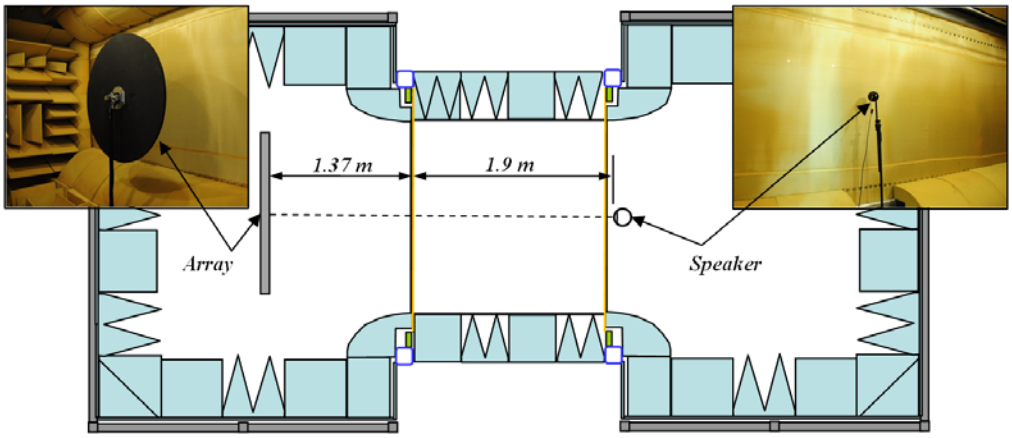

Figure 17. *Schematic of the test setup used to determine the losses associated to sound propagation through the Kevlar windows and boundary layer.*

As mentioned before, the losses due to propagation of sound through the Kevlar windows were obtained from the test with no flow. The attenuation was computed by comparing the average spectra of the microphones at the center of the array (i.e. 9 microphones in a 4in-diameter circle) to the data from the test with the speaker on the same chamber than the array (i.e. no losses). Since the speaker was behind two Kevlar walls, the attenuation was twice the desired value.

Figure 18 shows the noise attenuation spectrum obtained with a frequency resolution of 100 Hz and 800 averages. Insertion loss measurements by Jaeger et al. (2000) for the same kind of Kevlar used in the windows showed an oscillatory behavior as a function of frequency similar to the one observed in Figure 18. However, the Kevlar attenuation levels measured at the VT tunnel were slightly higher than the ones reported by Jaeger et al. for the thin Kevlar 120®, e.g. about 1.5 dB at 20KHz. A simplified quadratic curve fit of the results in Figure 18 renders the following equation for the Kevlar losses as a function of frequency, in Hz:

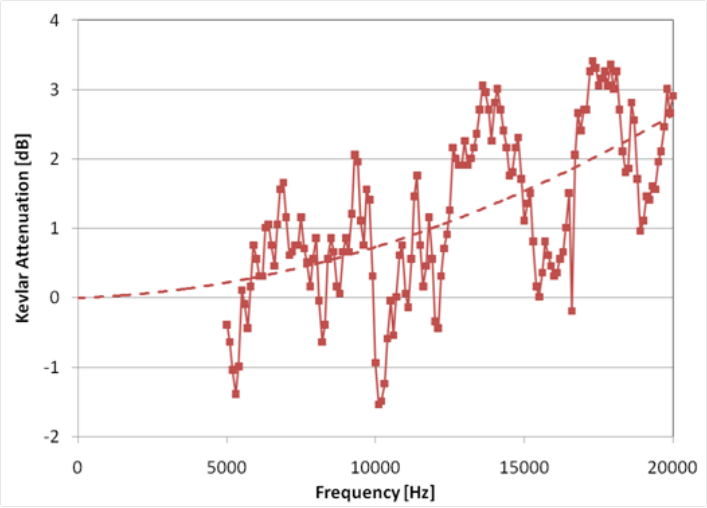

Figure 18. *Curve fit for Kevlar correction obtained from microphones spectra with 100Hz resolution.*

$$\Delta_{Kevlar}\,[dB] = 5.9\times10^{-3}\left(\frac{f}{1000}\right)^2 + 1.45\times10^{-2}\left(\frac{f}{1000}\right) \tag{15}$$

To determine the losses due to sound transmission through the boundary layer, the empty tunnel was run at 15, 30, 45, 60 and 75 m/s while the speaker was driven with white noise on the opposite anechoic chamber as explained before. The diffraction effects due to the flow were accounted for in the analysis. The spectra of these cases were then compared to the no-flow case to determine the attenuation due to the boundary layers. Since two boundary layers were present between the array and the speaker (one on each side of the test section), the correction for a single boundary layer is simply half the difference in levels observed between the no-flow and flow cases. The data showed that the speaker was not driven loudly enough at the highest flow speed to perform the analysis using the average spectrum of the microphones like in the case for the Kevlar. It was then decided to perform the analysis using the integrated spectra in 1/12th octave bands. Although the beamforming algorithm only accounts for the refraction effects on the boundary layer closer to the array, the errors introduced were expected to be small. These issues will be further addressed in the near future.

The attenuation due to the boundary layer showed dependence with frequency only below 3200Hz, e.g. attenuation rolls-off for lower frequencies. At higher frequencies, the boundary layer losses are mainly a function of flow speed. To determine this relation, the integrated spectra between 3200 and 7100 Hz was analyzed (see Figure 19). The attenuation at each flow speed, regardless of its frequency, was then plotted as a function of flow speed as shown by the symbols in Figure 20. The data was then curve fitted using a quadratic curve to obtain a "frequency average" boundary layer attenuation as a function of Mach number. The equation for the quadratic curve is given by:

$$\Delta_{BL-M}[dB] = 5.4316\,M + 88.95\,M^2 \qquad (16)$$

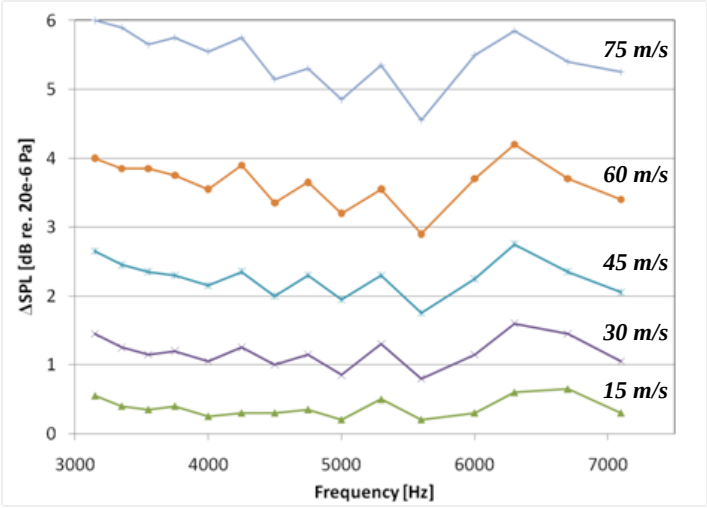

Figure 19. *1/12th octave bands integrated spectra at different flow speeds.*

To determine the attenuation as a function of frequency at the lower frequencies (<3200 Hz), the data obtained by Burdisso and Errasquin (2009) was used in conjunction with the data obtained here. The same exponentially increasing model for the frequency dependence of the attenuation below 3200 Hz was adopted here, i.e. $\left(1 - e^{-\beta f}\right)$ with $\beta = 0.001057$.

By incorporating the quadratic fit for the flow speed dependence at frequencies above 3200 Hz as described before and the low frequency dependence, the model used to account for boundary layer losses as a function of frequency and flow Mach number is given by:

$$\Delta_{BL}[dB] = \left(1 - e^{-\beta f}\right)(\alpha_1 M + \alpha_2 M^2) \qquad (17)$$

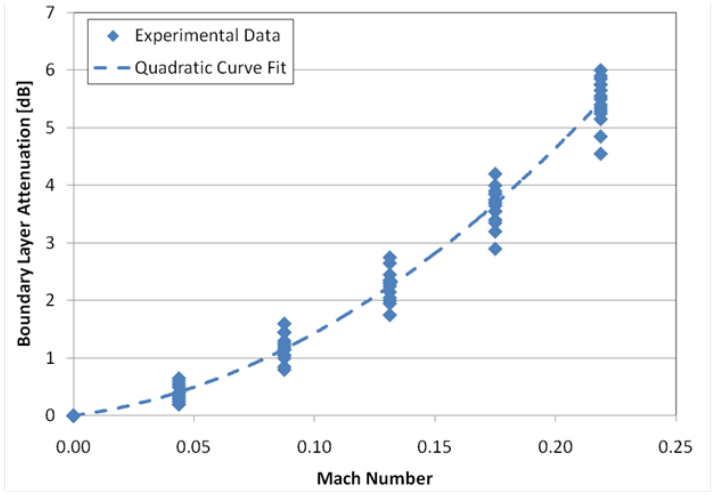

Figure 20. *Data and curve fit to obtain noise attenuation due to boundary layer transmission.*

with $\alpha_1 = 5.4316$, $\alpha_2 = 88.95$, and $\beta = 0.001057$. Sample corrections for Kevlar and boundary layer losses for 36 and 72m/s are plotted in Figure 21a. The total corrections (Kevlar plus boundary layer) for 36 and 72m/s are shown in Figure 21b.

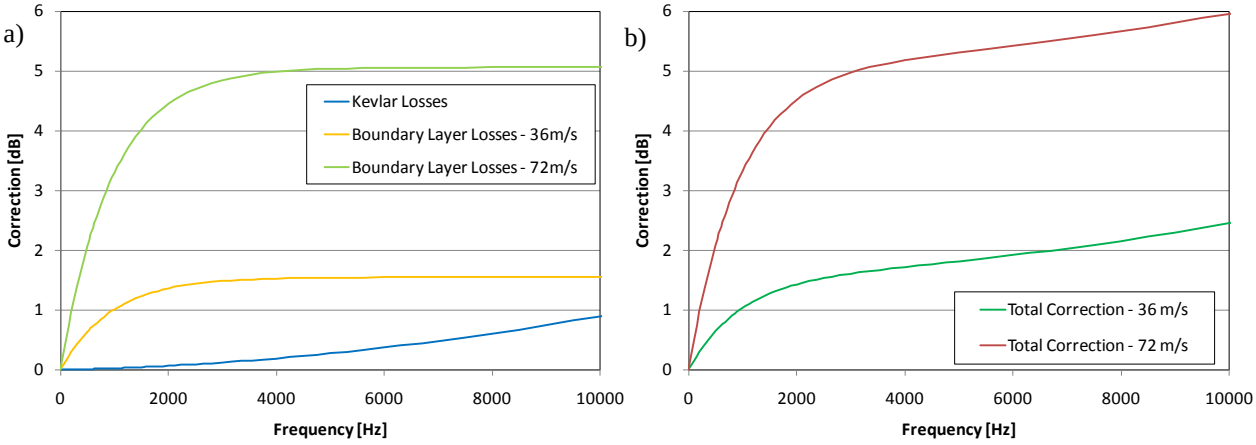

Figure 21. *a) Corrections for sound transmission through Kevlar windows and boundary layer. b)Total corrections for sound transmission through Kevlar windows and boundary layer*

VI. Benchmark Trailing Edge Noise Results

This section describes the experimental data used to benchmark the results obtained with a 0.2 m chord NACA0012 profile at the Virginia Tech Anechoic Wind Tunnel. In particular, the data is compared to results obtained at NASA by Brooks et al. (1989) and at the National Aerospace Laboratory of The Netherlands (NLR) by Oerlemans and Migliore (2004) for a 0.2286 m chord model. In addition, the noise from the large chord 0.91 m NACA0012 airfoil tested at high Reynolds numbers is compared to predictions. Details of each set of experimental tests are presented below.

C. Experimental data obtained by NASA

Brooks et al. (1989) performed experiments of six NACA 0012 airfoils of chord length ranging from 0.025 m to 0.3 m with a span of 0.45 m. The experiments were performed in an open jet wind tunnel. For each model, data were collected at various effective angles of attack ranging from 0° to 22°, depending on the airfoil, and various flow speeds ranging from 32 to 71 m/s for nominal chord Reynolds numbers of ~0.05 to ~1.4 million. Table 1 shows a summary of the cases tested. The data were collected with eight microphones distributed around the model. Then, the data was processed using a procedure based on correlation in order to eliminate the background noise and isolate the trailing edge noise component. The results were presented as the sound pressure level (L_p) corresponding to an observer's distance of 1.23 m normal to the plane that contains the chord and span lines when the airfoil is at 0° angle of attack. Noise spectra in 1/3rd octave frequency bands were published together with a semi-empirical prediction code. The frequency range of the experimental data varied according to the cases, ranging from 0.2 to 20 kHz. The data collected by Brooks et al. are only available in the corresponding publication as figures showing noise spectra for each airfoil for each condition. The experimental results shown here were obtained by digitizing the corresponding figures.

All tests were performed for conditions of clean and tripped leading edge. The tripping of the leading edge had the objective of forcing the development of a turbulent flow regime. The tripping of the boundary layer was achieved by a random distribution of grit in strips from the leading edge to 20% chord. This tripping was considered heavy because of its extension along the chord. The trailing edge bluntness of the models was constructed with a thickness of less than 0.05 mm which allows them to be treated as sharp trailing edges.

Aerodynamic flow measurements were performed using hot-wires. The boundary layer thickness was measured in the proximity of the trailing edge. For most cases, this measurement was made 1.3 mm downstream from the trailing edge. Experiments were reported to have an accuracy of 5% for turbulent cases and 10% for laminar or transitional cases. The boundary layer thickness, δ, displacement thickness, δ^*, and momentum thickness, θ, were calculated from the measured mean velocity profiles.

Table 1. *Ranges of flow speed and effective angle of attack tested by Brooks et al. (1989)*

Airfoil	Chord	Untripped		Tripped	
		Flow speed	Effective AoA	Flow speed	Effective AoA
	[m]	[m/s]	[deg]	[m/s]	[deg]
NACA 0012	0.025	32 to 71	0 to 12	32 to 71	0 to 22
NACA 0012	0.05	32 to 71	0 to 19	32 to 71	0 to 20
NACA 0012	0.1	32 to 71	0 to 15	32 to 71	0 to 16
NACA 0012	0.15	32 to 71	0 to 12	32 to 71	0 to 13
NACA 0012	0.23	32 to 71	0 to 7	32 to 71	0 to 7
NACA 0012	0.3	32 to 71	0 to 4	32 to 71	0 to 4

D. Experimental data obtained at NLR

Aeroacoustic tests of seven airfoils were performed at the National Aerospace Laboratory of The Netherlands (Oerlemans, 2004; Migliore and Oerlemans, 2004). The experiments were conducted in an open jet anechoic wind tunnel for several flow speeds and angles of attack. Seven airfoils were tested, including a 0.23m chord NACA 0012. The model had a span of 0.51 m. The trailing edge was built respecting tolerances that assure a blunt thickness lower than 0.375 mm. In the cases where the airfoil was tripped, the trips were located at 2% and 5% chord on the suction and pressure sides of the airfoil, respectively. The stream-wise peak-to-peak length of the zigzag tape used was 11 mm. The standard trip thickness was 0.25 mm, but for some cases trips of up to 0.5 mm were used.

Data were collected at various effective angles of attack ranging from 0° to 7°, and flow speeds ranging from 32 to 71 m/s. Table 2 shows a summary of the NACA0012 cases tested. The noise measurements consisted of far-field acoustic data using a 48-element microphone phased array system. The array was placed outside the tunnel's flow at a distance of 0.6 m from the model's rotating axis on the suction side of the airfoil. The integrated noise spectra were computed for a volume enclosing the central 0.1 m of the span. The results were reported as sound power level assuming a monopole behavior of the source in 1/3rd octave bands (Migliore and Oerlemans, 2004). Therefore, at a distance of 0.282 m the sound pressure level has the same value as the sound power level. The measurements were made in the frequency range from 80 to 20000 Hz. Nevertheless, the facility used was considered anechoic only above 500 Hz. Furthermore, the microphone array used was designed for maximum side-lobe suppression at frequencies between 1 and 20 kHz. Therefore, the data were assumed valid between 500 and 20000 Hz, with a higher accuracy above 1000 Hz.

Table 2. *Ranges of flow speed and effective angle of attack tested by NLR.*

Airfoil	Chord	Untripped		Tripped	
		Flow speed	Effective AoA	Flow speed	Effective AoA
	[m]	[m/s]	[deg]	[m/s]	[deg]
NACA 0012	0.23	32 to 71	0 to 7	32 to 71	0 to 7

E. Experimental data obtained at Virginia Tech (VT)

Under various programs, noise data for two NACA0012 models were obtained at Virginia Tech (*Devenport et al.*, 2008, Devenport *et al.*, 2010). These models have chord lengths of 0.2 and 0.91 m, respectively. Table 3 shows a summary of the NACA 0012 cases tested at VT. Data were collected at various effective angles of attack ranging from zero lift to stall condition, and various flow speeds ranging from 10 to 66 m/s for nominal chord Reynolds numbers of ~0.6 to ~3.8 million. Tests were also performed with boundary layer trips.

Table 3. *Ranges of flow speed and effective angle of attack tested at Virginia Tech.*

Airfoil	Chord	Untripped		Tripped	
		Flow speed	Effective AoA	Flow speed	Effective AoA
	[m]	[m/s]	[deg]	[m/s]	[deg]
NACA 0012 (2007 Test)	0.91	15 to 66	-8 to 5	10 to 66	-14 to 12
NACA 0012 (2009 Test)	0.91	28 to 54	-12 to 12	28 to 54	-12 to 12
NACA 0012 (2007 Test)	0.2	41 to 55	0 to 7	40 to 52	0 to 5

The models were designed to span the complete vertical height of the test section, i.e. 1.8 m. The tripping method for the results presented in this work consisted of serrated trip tape (Glasfaser-Flugzeug-Service GmbH 3D Turbulator Tape). The trip was applied along the entire span at the 10% chord location measured from the leading edge on both the airfoil suction and pressure sides. The tape has a thickness of 0.5 mm and an overall width of 12 mm.

In the 2007 tests, noise measurements were carried out with a 63-element microphone phased array located 3 m from the model as shown in Figure 22 (Devenport *et al.*, 2008). The data from the microphones in the array was processed to compute the acoustic maps over a plane along the center of the test section in the 500 to 5000 Hz range as shown in Figure 22.

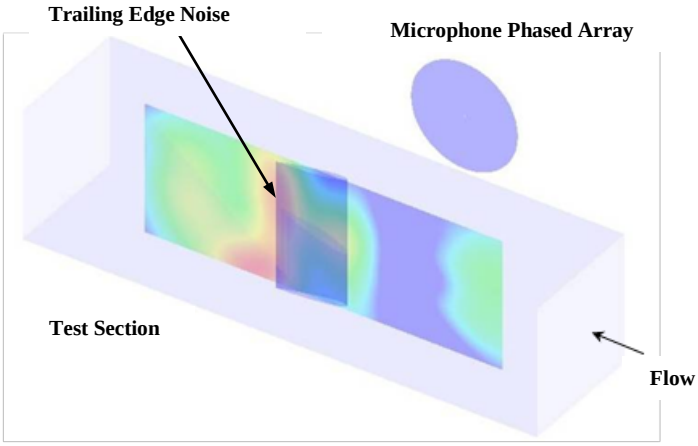

Figure 22. *Schematic of the NACA 0012 Airfoil inside the wind tunnel test section and a typical acoustic map. (Extracted from Devenport et al., 2008)*

Integrated spectra were computed over a volume enclosing the trailing edge of the airfoil. The parts of the trailing edge next to the junction with the tunnel were excluded from the integration region to avoid noise due to end effects as well as other spurious noise sources seen on the test section floor and ceiling. Therefore, the integrated spectra represent the trailing edge noise radiated by the center 2/3 of the airfoil as measured at the center of the array position. The noise measurements performed in 2009 followed the same procedure except that a new 117-element microphone phased array was used.

F. Summary of Experimental Data

Figure 23a shows the range of chord Reynolds numbers versus the range of angle of attacks covered for each NACA0012 airfoil tested for tripped cases. Each polygon represents a Reynolds number versus angle of attack envelope. It can be observed that the VT data (blue) cover the largest range, in particular towards the higher Reynolds numbers. A similar summary is shown for the untripped cases in Figure 23b.

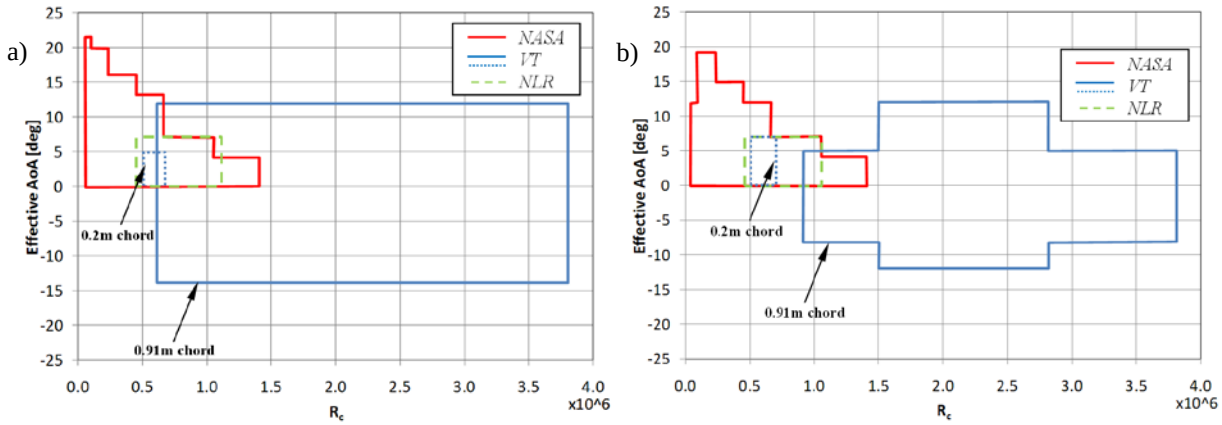

Figure 23. *Summary of Reynolds number versus angle of attack range for a) tripped and b) untripped NACA 0012 airfoils.*

G. Corrections Applied to the Experimental Data

In order to correctly compare the results, the experimental data were first adjusted to account for the different measurement methods, locations, airfoil chord, flow speeds, and processing. Firstly, the data from the different facilities were corrected to an observer position at 3 m from the trailing edge in the direction perpendicular to the plane containing the chord and span lines of the airfoil. The source airfoil span length was set at 1.22 m. These are the conditions corresponding to the VT tests for 0° effective angle of attack. Since radiation directivity effects are small (<1 dB) for the angle of attack tested, corrections for differences in directivity were not made for the VT and NLR data (Errasquin, 2009).

Secondly, the small-chord Virginia Tech data were corrected for the difference in chord (0.2 to 0.2286) and flow speeds to match the NASA conditions. The VT airfoil has a smaller chord (0.2 m) and the flow speeds were close but not exactly the same as the one tested by NASA. To this end, the Virginia Tech results were corrected for the difference in chord using the same normalization as Brooks *et al.* (1989). In practice, the code developed by Brooks *et al.* (1989) was run for both chord lengths and the results used to find the 1/3rd Octave band corrections. The 5th power law was then used to account for the small differences in flow speed. Note that the airfoil tested by NLR matched exactly the chord of the articles tested by NASA (0.2286 m) and were tested at the same flow speeds. Thus, the NLR data did not require these corrections.

H. Comparison of Results

Figure 24 shows a comparison of corrected results for two flow speeds and three angles of attack for the tripped case. In these plots, the black lines represent experimental data obtained at VT, the red lines correspond to the tests performed at NLR, and the blue lines were obtained at NASA. The dashed blue line was obtained using the semi-empirical prediction tool developed by Brooks *et al.* (1989). The untripped case was not compared since the vortex shedding noise mechanism is sensitive to small differences in geometry and tunnel conditions. The angles of attack reported in the figures are effective values, i.e. tunnel interference corrections were applied. It is interesting to mention that the ratio of the effective to geometric angle of attack for the NASA, NLR, and VT tunnels was 37%, 44%, and 95%, respectively, implying an order of magnitude smaller lift interference correction for the latter.

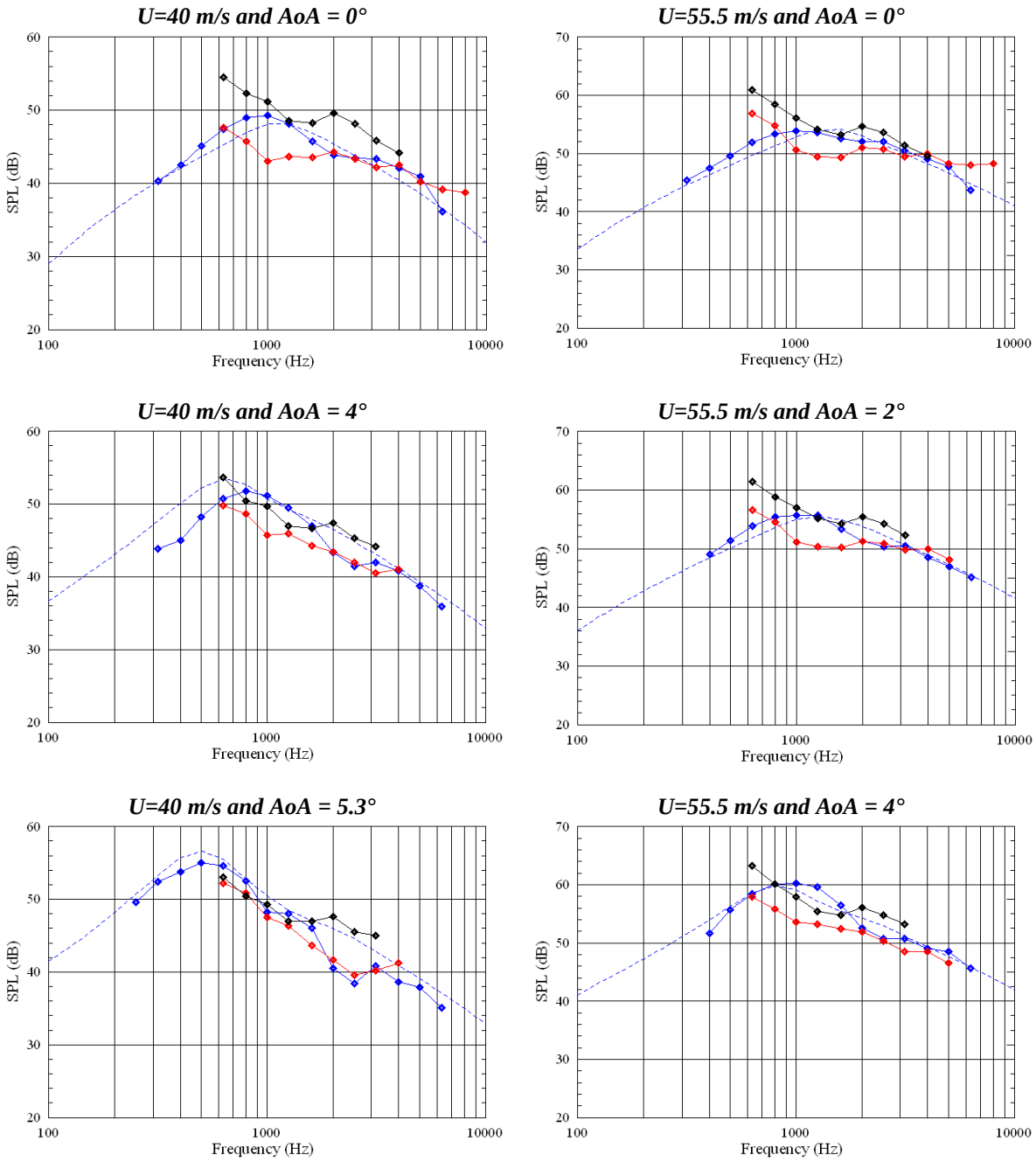

Figure 24. *Comparison of self noise spectra for 22.86 cm chord NACA0012 airfoil with tripped boundary layer measured at VT (♦——♦), NLR(♦——♦), and NASA (♦——♦ measured, ----- predicted). Note: NAFNoise predictions using semi-empirical boundary layer properties.*

The sample results in Figure 24 show that VT and NLR results show very similar spectral shape, but with an offset in terms of absolute levels. The VT and NLR spectral shape differs from the one measured by NASA. In particular, the NASA spectra show a broad peak centered on the 1000 Hz band while the VT and NLR the level continue increasing toward the lower frequency bands. Unfortunately, data below 500 Hz in both of these facilities is not available. It was speculated that a possible cause for the 1kHz peak observed by NASA was due to extraneous noise sources at the junction of the model and the endplates used in the tests that the two-microphone technique used

could not discern from the trailing edge noise (Oerlemans, 2004). The similar trend of the VT and NLR results give some credibility to this argument. In terms of absolute levels, the VT data is for the most part about 4 dB louder than the NLR data. In general, the NASA data positioned in between the VT and NLR results. The largest discrepancy in the data occurs for the 40 m/s and 0° AoA where the VT results differ more markedly, e.g. levels are clearly higher than the NLR and NASA. In summary, it is rather remarkable that the data from three different tunnels, using different models, tripping methods, and measurement techniques yields very similar results. For the most part, all the results are within a range of 5 dB.

As shown in Figures 23a and b, the tests using the Virginia Tech 0.91 chord NACA0012 airfoil is the only data set providing results at high Reynolds numbers. Thus, Figure 26 show the comparison between the 0.91m chord NACA0012 tested at VT and the predictions obtained using the software NAFNoise (Moriarty, 2005). The self-noise prediction tool in this software is based on an improvement of the semi-empirical method developed by Brooks *et al.* (1989). In NAFNoise, the semi-empirical boundary layer thickness formulae used by Brooks was replaced by the prediction routine Xfoil (Drela, 2001). This code was validated with experimental data for small airfoils, i.e. low Reynolds numbers. In addition, it was compared to the predictions using the original method developed by Brooks et al. (1989). It was reported that the new prediction method improved the predictions, in particular at low angles of attack (0 to 5°) over a frequency range between 1-4 kHz (Moriarty *et al.*, 2004).

The results in Figure 25 compare the measured and predicted self noise for four angles of attacks from 0° to 9° at three flow speeds corresponding to chord Reynolds numbers in the 1.5 to 2.8 million range. It is observed that the predictions over predict the measured levels in all cases. The over prediction is about 3-5dB for low AoAs, reaching up to 10dB for high AoAs. These differences also seem to increase at higher frequencies. The lack of agreement between predictions and measurements is most likely due to the fact that the predictions are based on extrapolating low Reynolds number results (red box in Figure 23a) to much larger values (blue box in Figure 23a).

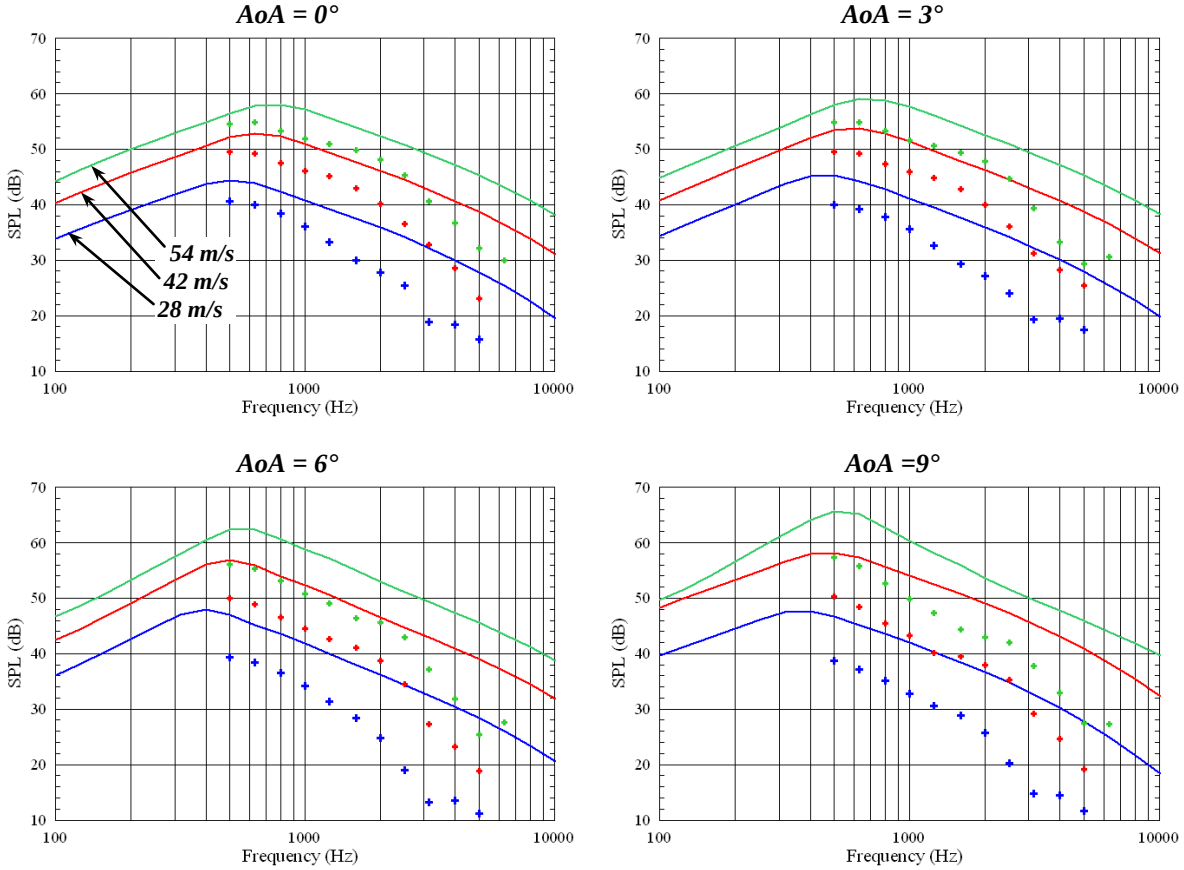

Figure 25. *Comparison of self noise spectra for 91.4 cm chord NACA0012 airfoil with tripped boundary layer measured at VT (dots) and predicted using NAFNoise code (solid lines).*
Note: *NAFNoise prediction using Xfoil to estimate boundary layer properties.*

VII. Conclusions

A detailed study has been made of the aerodynamic and acoustic characteristics of a large-scale Kevlar-walled anechoic wind tunnel. It is found that:

- flow along the porous test section walls is well behaved and remains attached even when testing a large airfoil at high angle of attack,
- lift interference effects, associated with transpiration through the Kevlar walls, are an order of magnitude smaller than in an open-jet configuration and can be accurately corrected for using a simple analysis based on the independently measured through-flow characteristics of the Kevlar fabric,
- blockage effects are a fraction of those which would be experienced in an equivalent hard-wall test section and appear, in many cases, to be negligible,
- the facility is anechoic above 180Hz,
- the attenuation of sound passing through the Kevlar walls is less than 1dB below 10kHz and smaller than that associated with test section boundary layer of about 1.5 and 5dB at 36 and 72m/s respectively
- NACA 0012 trailing edge noise measurements made in the facility at comparable conditions are closely consistent with the earlier results of Brooks *et al.* (1989) and Oerlemans (2004),
- trailing edge noise radiated by a NACA 0012 airfoil at chord Reynolds numbers from 1.5 to 2.8 million is significantly overpredicted by the standard semi-empirical prediction method.

Acknowledgments

This work was performed under sponsorship from Sandia National Laboratories (PO 872540), GE Global Research (PO 400017513) and NREL (ZAM-4-33226-01). We would also like to gratefully acknowledge the advice and support of Drs. Anurag Gupta, Kevin Kinzie, Trevor Wood (GE), Dr. Dale Berg (Sandia), and Drs. Pat Moriarty and Paul Migliore (NREL), in performing these studies.

References

1. Allen H.J. and Vincenti W.G.,"Wall interference in a two-dimensional-flow wind tunnel, with consideration of the effect of compressibility." NACA Report No. 782, 1947.
2. Bies D.A. and Hansen C.H., *Engineering Noise Control: Theory and Practice*, Academic Division of Unwin Hyman, Ltd. London, UK, 1988.
3. Björck, A., "Numerical methods for least squares problems," Society for Industrial and Applied Mathematics (SIAM), Philadelphia, 1996.
4. Brooks T F, Pope D S and Marcolini, "Airfoil Self Noise and Prediction", NASA RP 1218, 1989.
5. Burdisso, R.A. and Errasquin L., "Calibration of the Virginia Tech Anechoic Wind Tunnel for the Corrections of Airfoil Noise Data," Final Report for Sandia National Labs, Virginia Tech, April 2009.
6. Devenport W.J., Borgoltz A., Burdisso R.A., Ravetta P. and Macko N., "Tests of Trailing Edge Modifications to a G.E. Wind Turbine Blade Section," Final Report to G.E. Global Research, Virginia Tech, January 2010.
7. Drela, M, 2009, "Xfoil subsonic airfoil development system", http://web.mit.edu/drela/Public/web/xfoil/
8. Ewald B.F.R. (Editor), "Wind Tunnel Wall Correction", AGARDograph 336, October 1998.
9. Errasquin L.A., "Airfoil Self-Noise Prediction Using Neural Networks for Wind Turbines," Master of Science Thesis, Mechanical Engineering, Virginia Tech, September 2009.
10. Kelley C. T., Iterative Methods for Optimization, Society for Industrial and Applied Mathematics (SIAM) Frontiers in Applied Mathematics, no 18, 1999.
11. Legouias T. and Nicolas J., "Phase gradient method of measuring the acoustic impedance of materials," J. Acoustical Society of America, 81(1), January 1987.

12. Oerlemans, S., Wind Tunnel Aeroacoustic Tests of Six Airfoils for Use on Small Wind Turbines, National Aerospace Laboratory, Emmeloord, The Netherlands, NREL SR-500-34470, 2003.

13. Migliore, P.J. and Oerlemans, S., "Wind Tunnel Aeroacoustic Tests of Six Airfoils for Use on Small Wind Turbines," AIAA Wind Energy Symposium, Reno, Nevada, January 5–8, 2004.

14. Moriarty P.J., Guidati G., and Migliore P.G., "Recent Improvement of a Semi-Empirical Aeroacoustic Prediction Code for Wind Turbines," AIAA 2004-3041, 10th AIAA/CEAS Aeroacoustics Conference, Manchester, UK, AIAA 2004-3041, 2004.

15. Moriarty P., "NAFNoise user's guide," NWTC Design Codes, National Renewable Energy Laboratory, Golden, CO, USA, http://wind.nrel.gov/designcodes/simulators/NAFNoise/, 2005.

16. Remillieux M.C., Crede E.D., Camargo H.E., Burdisso R.A., Devenport W.J., Rasnick M., Van Seeters P., and Chou A., "Calibration and Demonstration of the New Virginia Tech Anechoic Wind Tunnel," AIAA-2008-2911, 14th AIAA/CEAS Aeroacoustics Conference (29th AIAA Aeroacoustics Conference), Vancouver, British Columbia, May 5-7, 2008.

17. Smith B, Camargo H, Burdisso R and Devenport W, 2005,"Designand Testing of a Novel Acoustic Wind Tunnel Concept", AIAA paper 2005-3053, 11th AIAA/CEAS Aeroacoustics Conference, May 23-25, 2005, Monterey CA.

18. Wong C.C., Soetrisno M., Blottner F.G., Imlay S.T., and Payne J.L., "PINCA: A scalable parallel program for compressible gas dynamics with nonequilibrium chemistry", Sandia National Labs Report SAND 94-2436, Albuquerque, NM, April 1995.